


Article

Open Access



Exploring the interplay of Ti-Sn co-doping in photoelectrochemical water splitting of hematite nanowires

Francisco Javier Fernández-Alonso^{1,2,3}, Paula Quiterio⁴, Rui Vilarinho⁴, João P. Araújo⁴, Adélio Mendes⁵, Miguel Manso-Silván^{1,2,3}, Vicente Torres-Costa^{1,2}, Arlete Apolinario⁴, Célia Tavares de Sousa^{1,2,3} 

¹Departamento de Física Aplicada, Facultad de Ciencias, Universidad Autónoma de Madrid, Madrid 28049, Spain.

²Instituto "Nicolás Cabrera", Facultad de Ciencias, Universidad Autónoma de Madrid, Campus de Cantoblanco, Madrid 28049, Spain.

³Centro de Microanálisis de Materiales, Universidad Autónoma de Madrid, Madrid 28049, Spain.

⁴IFIMUP - Institute of Physics for Advanced Materials, Nanotechnology and Photonics of University of Porto, Departamento de Física e Astronomia, Faculdade de Ciências, Universidade do Porto, Porto 4169-007, Portugal.

⁵LEPABE - Faculdade de Engenharia, Universidade do Porto, Porto 4200-465, Portugal.

*Correspondence to: Dr. Célia Tavares de Sousa, Departamento de Física Aplicada, Facultad de Ciencias, Calle Francisco Tomás y Valiente 7, M12-104, Madrid 28049, Spain. E-mail: celia.tsousa@uam.es

How to cite this article: Fernández-Alonso, F. J.; Quiterio, P.; Vilarinho, R.; Araújo, J. P.; Mendes, A.; Manso-Silván, M.; Torres-Costa, V.; Apolinario, A.; de Sousa, C. T. Exploring the interplay of Ti-Sn co-doping in photoelectrochemical water splitting of hematite nanowires. *Energy Mater.* **2025**, *5*, 500136. <https://dx.doi.org/10.20517/energymater.2024.108>

Received: 4 Aug 2024 **First Decision:** 11 Nov 2024 **Revised:** 18 Jan 2025 **Accepted:** 25 Jan 2025 **Published:** 15 Jul 2025

Academic Editor: Wei Tang **Copy Editor:** Ping Zhang **Production Editor:** Ping Zhang

Abstract

Photoelectrochemical water splitting is a promising alternative for sustainable energy production, addressing the growing need for clean energy sources. Hematite is a potential semiconductor for this process due to its abundance, low cost, non-toxicity, and stability. However, bare-hematite-based photoelectrochemical cells face challenges such as low photocurrent density, requiring innovative strategies to improve efficiency. This study explores the combined effects of three key approaches: enhancing crystallinity through high-temperature annealing, increasing specific surface area via nanostructuring, and improving photoanode conductivity through heteroatom doping. Hematite nanowires were synthesized using a hydrothermal method, with Ti-doping introduced during hydrothermal synthesis and subsequent Sn co-doping during an 800 °C annealing process, which also improved crystallinity. The introduction of Ti dopant significantly increased the photocurrent density under simulated solar illumination from 0.03 mA·cm⁻² to 0.63 mA·cm⁻². Co-doping with Ti and Sn further enhanced performance to 1.27 mA·cm⁻². The research explores how heteroatom doping influences the properties of hematite and examines its interaction with high-temperature annealing. These findings are significant for advancing the



© The Author(s) 2025. **Open Access** This article is licensed under a Creative Commons Attribution 4.0 International License (<https://creativecommons.org/licenses/by/4.0/>), which permits unrestricted use, sharing, adaptation, distribution and reproduction in any medium or format, for any purpose, even commercially, as long as you give appropriate credit to the original author(s) and the source, provide a link to the Creative Commons license, and indicate if changes were made.



design of efficient nanostructures for energy conversion applications.

Keywords: Hematite, hydrogen production, heteroatom doping, nanostructuring, photoelectrochemistry, photoanodes

INTRODUCTION

In recent years, rapid industrial growth and societal development have led to a significant increase in fossil fuel consumption^[1]. Consequently, the world faces two major challenges: environmental pollution and energy resource depletion^[2,3]. Direct production of hydrogen from renewable resources such as sunlight and water using a photoelectrochemical (PEC) cell holds promise as a cost-effective approach for harvesting and storing solar energy^[4]. The use of hematite ($\alpha\text{-Fe}_2\text{O}_3$) photoanodes in PEC water splitting has attracted significant interest because of its abundance, very good long-term stability^[5], and appropriate bandgap (about 2.2 eV), theoretically enabling a solar-to-hydrogen conversion efficiency of 16.8%^[6-8]. However, pure-hematite-based PEC cells suffer from low photocurrent density and large overpotential, primarily due to hematite's poor conductivity and short hole diffusion length, resulting in high electron-hole recombination and efficiency losses^[9].

To improve the hematite photocurrent density, two parameters can be manipulated: recombination reaction time (τ_r) and carrier (hole or electron) drift time (τ_d). Increasing τ_r (reducing recombination rate) can be achieved by passivating surface states to diminish the positive charge accumulation on the surface^[10]. Additionally, improving crystallinity by reducing the number of grain boundaries, which act as non-radiative recombination centers, through thermal annealing processes is beneficial^[11-13]. Conversely, decreasing τ_d (accelerating carrier extraction) involves reducing carrier migration distance and enhancing carrier mobility to boost the built-in field.

Nanostructuring significantly enhances PEC performance by expediting photogenerated carrier extraction and improving charge separation^[14,15]. Nanostructuring results in benefits such as larger surface area, better light absorption, reduced electron-hole recombination, and enhanced electronic properties due to quantum confinement effects^[16-18]. Notably, the one-dimensional structure of nanowires (NWs), influenced by quantum confinement, shifts the absorption spectrum towards the visible range, thereby enhancing photoactivity.

The inclusion of impurity atoms, whether intentionally or unintentionally, within the hematite lattice has been demonstrated to significantly enhance photocurrent^[12,19]. Incorporating high concentrations (ranging from 0.5% to 20% atomic) of impurities such as Si^[20], Sn^[11], Se^[21], Cr^[22], Pt^[23], Mn^[24], Cr^[25], Ge^[26], W^[27] or Rh^[28] has been achieved mostly through physical and chemical deposition, spray pyrolysis, or hydrothermal techniques^[6,8,20,29-32]. Also, it has been shown that surface modification of hematite photoanodes can contribute to improving their PEC properties^[33-36]. While most dopants yield modest improvements in PEC performance of hematite photoanodes, notable enhancements have been observed with Si, Ti and Sn doping^[37]. In many studies, dopants are introduced into nanostructured hematite during the material growth process, allowing control over doping concentration. Particularly, Ti doping via hydrothermal techniques has become a primary method for improving hematite photocurrent by increasing donor density and carrier density, thus leading to higher solar-to-hydrogen conversion efficiency^[38,39].

While some studies have addressed Ti-doping^[8,40-42], most do not delve deeply into understanding the influence of Ti on the nanostructure. Furthermore, the high-temperature annealing strategy can

unintentionally dope the hematite photoanodes with Sn^[11,12,43]. Although the effect of Sn doping has been explored, the interaction between Sn and Ti through intentional crossover doping has not been studied.

In this study, three strategies were combined to enhance hematite photoanode performance: (i) optimization of thermal annealing to enhance separation efficiency by increasing τ_1 , (ii) nanostructuring to decrease τ_2 by reducing carrier migration distance and improving specific surface area, and (iii) dual-doping to enhance carrier mobility, thereby increasing τ_1 and reducing τ_2 . For this purpose, hematite NWs obtained through the hydrothermal method were doped with Ti in a controlled manner during photoanode fabrication, while Sn-doping was achieved through Sn⁴⁺ incorporation into the hematite structure from the fluorine-doped tin oxide (FTO) substrate during thermal annealing^[12].

This work aims to understand how the different strategies described above contribute to improving the efficiency of hematite photoanodes. For this purpose, this study successfully characterizes the impact of annealing conditions on dual doping with Ti and Sn and their interactions within the in-depth concentration profile using Rutherford Backscattering Spectroscopy (RBS). Moreover, the PEC performance evaluation of the photoanodes was conducted by determining the photocurrent density-voltage (*J-V*) curves and studying the incident photon-to-current efficiency (*IPCE*) as a function of wavelength. A comprehensive characterization of the photoanodes was also performed to better understand how each variable contributes to improving PEC cell efficiency. To this end, morphology was analyzed using field emission scanning electron microscopy (FE-SEM), composition was determined via X-ray photoelectron spectroscopy (XPS) and RBS, microstructure through X-ray diffraction (XRD) and Raman spectroscopy, and electrical properties using photoelectrochemical impedance spectroscopy (PEIS).

EXPERIMENTAL

Photoanodes synthesis

α -Fe₂O₃ NWs, with and without Ti doping, were prepared by hydrothermal method^[44]. FTO coated glass substrates (Solaronix, Aubonne), with dimensions 1.2 × 2.5 cm², were previously cleaned as reported by Francisco *et al.*^[45]. 7 Ω-square⁻¹ and 10 Ω-square⁻¹ substrates were used for the samples that followed the one-step and two-step annealing process, respectively, since the 7 Ω-square⁻¹ substrates were deformed when the high temperature annealing step was applied. Two schemes of samples were prepared by hydrothermal process (i) to obtain bare hematite NWs and (ii) Ti-doped hematite NWs. (i) FTO substrates were immersed in a stainless steel autoclave with 20 mL solution of 0.15 M FeCl₃·6H₂O and 1 M NaNO₃, adjusted at pH 1.5 with HCl 37%^[11,12], and heated at 95 °C for 4 h^[15]. (ii) In the case of Ti-doped samples, FTO substrates were also immersed in the solution (i), after adding 10 μL of Ti isopropoxide. Afterward, the samples were heated at 95 °C for 13 h (based on the procedure described by Yang *et al.*^[12,46]). All reagents were bought from Sigma-Aldrich.

Two annealing treatment approaches were studied: the one-step annealing approach, which involves annealing at 600 °C for 3 h, and the two-step annealing approach, which includes a first step at 550 °C for 2 h, followed by a short annealing step at 800 °C for 20 min^[12]. As-prepared samples with and without Ti dopant were subjected to both the one- and two-step annealing approaches. For Ti-doped samples, after the thermal annealing, the samples were again placed in an autoclave with solution (i) and heated at 95 °C for 20 min^[46]. The undoped one- and two-step annealed samples are denoted as 600PA and 800PA, respectively, while the doped samples are denoted as Ti600PA and Ti800PA, respectively.

Photoanodes characterization

Morphological characterization

The morphological characterization was performed using FE-SEM (FEI Quanta 400 ESEM FEG, FEI, Oregon) at CEMUP, University of Porto. The diameter (D) and thickness of NWs were estimated using ImageJ software^[47].

Structural characterization

The structural analysis was performed using XRD (Rigaku SmartLab, Rigaku, Tokyo) with Cu K α radiation (1.540593 Å) in parallel-beam mode with grazing incidence omega angles. Measurements were made in a 2θ range from 20° to 80°, with 0.02° increments and 0.5 s accumulation time. Raman spectroscopy was also used to confirm the crystalline phase and ordering of the photoanodes. The Raman scattering was measured using a Renishaw inVia Qontor Spectrometer, using an excitation laser with a 633 nm polarized line of He-Ne, in the spectral range from 200 cm⁻¹ to 1,400 cm⁻¹, an exposure time of 60 s and power of 1.1 mW. The diffraction patterns were refined by applying a Rietveld Refinement process, using the Match software (Crystal Impact, Bonn).

Surface compositional characterization.

To study the surface composition of the samples, XPS characterization was carried out. A Phoibos 150 EP MCD analyzer was used (SPECs Group, Berlin). The undoped 800 °C sample was irradiated with Al K α X-rays ($h\nu = 1486.6$ eV), while for Ti-doped samples, a Mg K α X-rays ($h\nu = 1253.6$ eV) source was used. According to the Seah and Dench model for inorganic compounds^[48], sampling depths of 9.6 nm and 9.0 nm have been estimated when using Al and Mg K α X-rays, respectively. The take-off angle was fixed at 90° to the sample surface. Pass energies of 50 eV and 20 eV were used for the survey and core level spectra, respectively. The binding energy (BE) values were corrected for charging effects by referencing the adventitious carbon C 1s peak, at 284.8 eV.

Bulk compositional characterization

On the other hand, to obtain additional information about the bulk composition, thickness and roughness, Rutherford ion backscattering experiments were performed with a 5 MV terminal voltage Tandetron accelerator located at “Centro de Microanálisis de Materiales”^[49]. Experiments were conducted using a 4.260 MeV He⁺ beam. The experiment was performed at normal incidence; backscattered ions were detected at 170°, and a cumulative charge of 12 μ C was collected. The experimental spectra were fitted using the SIMNRA 7.03 software^[50].

Photoelectrochemical impedance spectroscopy

The electrical properties of the photoanodes were examined by PEIS. In this technique, a small sinusoidal potential perturbation is applied to the system and the amplitude and phase shift of the resulting current response are recorded. A BioLogic SP-150 potentiostat (Bio-Logic, Seyssinet-Pariset, France) was employed. A frequency range between 0.1 Hz and 100 kHz was covered with a modulation signal of 10 mV^[55]. The EIS spectra were then fitted to an appropriate electrical equivalent circuit using ZView software (Scribner Associates Inc., Southern Pines).

Photoelectrochemical performance

The PEC performance of the hematite photoanodes was assessed based on the J - V curves, stability tests, intrinsic solar-to-chemical (ISTC) conversion efficiency, and IPCE measurements.

The photocurrent J - V curves were performed using a class B solar simulator with a 150 W Xe lamp (Oriel, Newport) under dark and 1-sun simulated sunlight ($100 \text{ mW}\cdot\text{cm}^{-2}$, AM 1.5 G). The photoanodes were immersed in 1.0 M NaOH electrolyte solution using a “cappuccino” PEC cell^[5,51], with an illuminated surface area of 0.528 cm^2 and a three-electrode configuration: Ag/AgCl/saturated KCl electrode as the reference electrode, a platinum wire as the counter-electrode and the hematite NW photoanodes as the working electrode. The photocurrent was assessed under front-side illumination, which resulted in higher photocurrent than backside illumination, as the transport of generated electrons from the illuminated hematite through the FTO layer is easier than transport of holes (with a short diffusion length of 2-4 nm) through the hematite layer^[12,52,53].

The stability tests were performed at a constant voltage of $1.23 V_{\text{RHE}}$ (voltage vs. reversible hydrogen electrode) for two hours, using the same conditions described above. The *ISTC* conversion efficiency was determined from the photocurrent density vs. potential curves measured under dark and illumination, in a three-electrode configuration^[5,54]. According to Rothschild’s model^[54], the *ISTC* is defined by

$$\begin{aligned} \text{ISTC} &= \left[\eta_{\text{el}} \frac{J_{\text{photo}}(\text{mA}\cdot\text{cm}^{-2}) \times V_{\text{photo}}(\text{V})}{P_{\text{light}}(\text{mW}\cdot\text{cm}^{-2})} \right]_{\text{AM1.5G}} \\ &\cong \frac{1.23(V_{\text{RHE}})}{U_{\text{dark}}(V_{\text{RHE}})} \left[\frac{J_{\text{photo}}(\text{mA}\cdot\text{cm}^{-2}) \times V_{\text{photo}}(\text{V})}{100(\text{mW}\cdot\text{cm}^{-2})} \right]_{\text{AM1.5G}} \end{aligned} \quad (1)$$

with η_{el} the electrolysis efficiency, J_{photo} the generated photocurrent, V_{photo} the correspondent photopotential and U_{dark} the potential applied to the photoanode to reach the respective dark current^[5,54]. Furthermore, the intrinsic photovoltaic power P_{light} for the photoanodes is given by

$$P_{\text{light}}(\text{mW}\cdot\text{cm}^{-2}) = J_{\text{photo}}(\text{mA}\cdot\text{cm}^{-2}) \times V_{\text{photo}}(\text{V}) \quad (2)$$

Also, the fill factor (*FF*) at the maximum power point (*MPP*) is determined by

$$\text{FF} = \frac{V_{\text{MPP}} \times J_{\text{MPP}}}{V_{\text{OC}} \times J_{\text{SC}}} \quad (3)$$

where V_{MPP} and J_{MPP} indicate the values of photopotential and photocurrent at the *MPP*, respectively; V_{OC} and J_{SC} represent the open circuit voltage and short circuit current, respectively.

IPCE measurements were carried out using a 150 W continuous-wave Xe lamp, with a computer-controlled monochromator. A scan was performed for wavelengths between 330 nm and 650 nm. The scanning speed was 2 nm/s. Measurements were performed at $V_{\text{RHE}} = 1.45 \text{ V}$. The *IPCE* can be calculated from the photocurrent measured at each wavelength, based on the expressions proposed in previous reports^[4,7].

RESULTS AND DISCUSSION

Morphological characterization

The morphology of the prepared photoanodes was assessed through FE-SEM, as shown in Figure 1A-F. The as-prepared NWs were observed to be fully formed during the initial stage of the autoclaving process. This formation is attributed to the thermodynamically stable nucleation of Fe^{3+} ions in solution, under controlled temperature and pressure conditions^[44].

For the undoped samples, following a one-step annealing process at 600 °C, the NWs exhibited a rounder morphology. Furthermore, the D of the NWs notably increased when subjected to a second annealing step

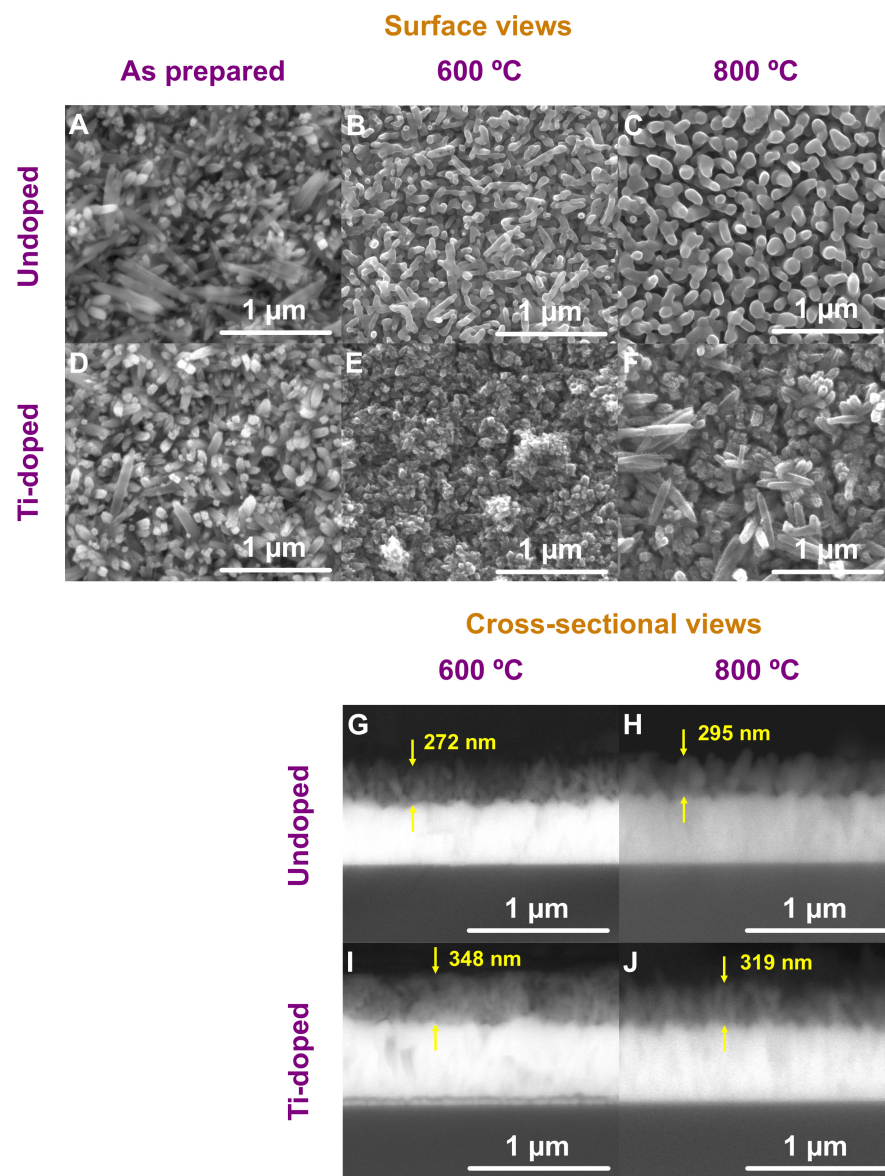


Figure 1. FE-SEM surface images of (A) undoped NWs after hydrothermal synthesis; and after (B) one-step and (C) two-step annealing processes; (D) Ti-doped NWs after hydrothermal synthesis, and after (E) one-step and (F) two-step annealing processes; Cross-sectional views of undoped (G) one-step and (H) two-step annealed, as well as Ti-doped (I) one-step and (J) two-step annealed α -Fe₂O₃ NWs. FE-SEM: Field emission scanning electron microscopy; NWs: nanowires.

at 800 °C for 20 min. Specifically, *D* measurements from top-view FE-SEM images revealed an increase from 63 ± 9 nm to 97 ± 19 nm when considering the one-step and the two-step annealing processes, respectively. The observed increase is attributed to the fusion between neighboring NWs during the high-temperature annealing step^[11,12,56].

In the case of Ti-doped photoanodes, a less ordered structure was obtained after one-step annealing at 600 °C compared to the undoped samples. In fact, the morphology and ordering of the NWs reflects a more random arrangement of hematite nanoparticles. Similar effects have been reported in previous works^[57,58]. Moreover, the trend observed in undoped samples regarding NW diameter dimensions persisted for the

Ti-doped samples in both annealing schemes: D increased from 46 ± 15 nm to 79 ± 8 nm when employing the two-step annealing process.

Figure 1G-J shows FE-SEM cross-sectional views of the samples. The thickness of the hematite photoanodes was estimated, revealing that for the undoped samples, the hematite layer measures approximately 272 nm after annealing at 600 °C. The thickness slightly increases to 295 nm following the final annealing step. In contrast, Ti-doped samples exhibit a higher thickness of about 348 nm when annealed at 600 °C. However, the high-temperature annealing step at 800 °C reduces the thickness in this case to 319 nm. In any case, the determination of the thickness of the hematite layer for such inhomogeneous samples is subject to a considerable margin of uncertainty. It can also be observed that in the case of the Ti-doped samples, the structure is more spongy and less ordered than in the case of the undoped ones, consistent with what was observed from the surface views.

Structural analysis

Figure 2 shows the XRD patterns for both bare and Ti-doped hematite NWs, subjected to the one- and two-step annealing schemes. It is observed that, for all the samples, the diffraction pattern contains peaks associated with the crystalline phase of hematite (α -Fe₂O₃), as well as with the main peaks of the FTO substrate. In all cases, the (110) diffraction peak predominates, suggesting that the crystallites are highly oriented vertically with respect to the substrate. Supplementary Table 1 shows the ratio between the intensity of the (110) and (104) diffraction peaks. This ratio is higher for the 800 °C annealed samples than for the 600 °C annealed samples, as well as for the undoped samples compared to the doped ones. This is consistent with what has been reported in the literature and confirms that the incorporation of Ti during the hydrothermal synthesis reduces the selectivity of the nucleation, leading to a more random distribution, in agreement with SEM images^[58-60].

The α -Fe₂O₃ lattice structure consists of an alternation of iron bilayers and oxygen layers, aligned parallel to the (001) basal plane. Within each bilayer, Fe³⁺ atoms have parallel spins, while the spins in adjacent bilayers are antiparallel^[61,62]. Electrons can move by hopping within the iron bilayers, but electron exchange between neighboring bilayers is spin forbidden by Hund's rule. Consequently, the conductivity of hematite is found to be four orders of magnitude higher within the (001) basal plane (e.g., in [110] direction) than in the orthogonal directions^[61,62]. Therefore, having a preferential orientation of the crystallites along the [110] direction is expected to enhance the efficiency of the PEC process^[63].

In addition to the peak associated with plane (110), the peaks associated with planes (102), (104), (113), (204), (116), (108), (214) and (300) can be also appreciated.

The crystallite size D and inhomogeneous strain ϵ have been estimated for each sample using the Williamson-Hall model^[64,65], as explained in the supplementary information. Williamson-Hall plots are shown in Supplementary Figure 1. With the two-step annealing scheme, an increase from $D = 27 \pm 4$ nm to $D = 37 \pm 12$ nm for the undoped and from $D = 23 \pm 3$ nm to $D = 30 \pm 5$ nm for the Ti-doped photoanodes is observed. This is ascribed to the hematite crystallinity improvement promoted by temperature^[11,13,29]. For Ti-doped samples, smaller crystallites were obtained, as previously reported by other authors^[59,66]. Also, the inhomogeneous strain has been estimated in $\epsilon = 0.06 \pm 0.05$ %, $\epsilon = 0.11 \pm 0.08$ %, $\epsilon = 0.06 \pm 0.04$ %, and $\epsilon = 0.12 \pm 0.05$ % for the 600PA, 800PA, Ti600PA, and Ti800PA photoanodes. Therefore, the 800 °C annealed samples present a slightly higher strain than the 600 °C samples. The greater strain for the 800 °C annealed samples than for the 600 °C annealed samples can be due to a greater incorporation of Sn⁴⁺ in the α -Fe₂O₃ structure at the interface with the FTO when the annealing temperature is higher. However, since

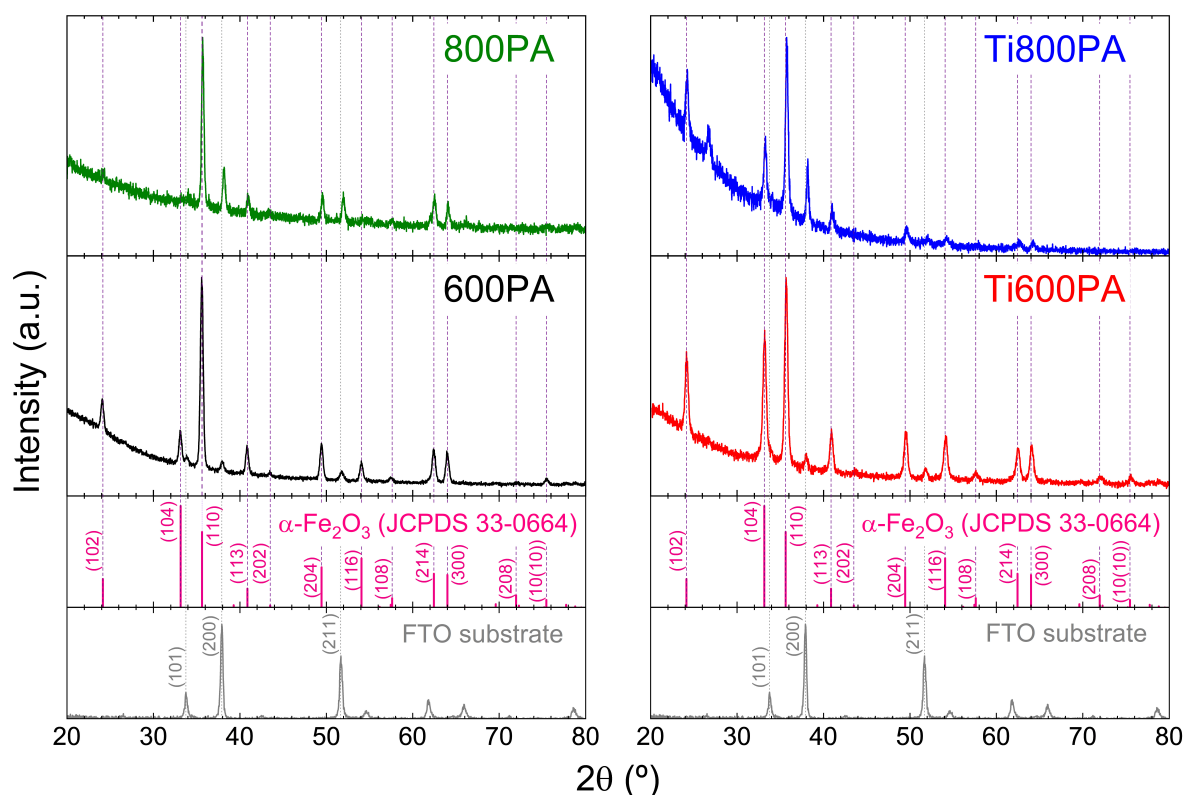


Figure 2. XRD patterns of the undoped and Ti-doped hematite NWs, subjected to one-step (600 °C) and two-step (800 °C) annealing processes. The α -Fe₂O₃ reference pattern (JCPDS 33-0664), and the diffractogram corresponding to the FTO substrate are also shown. XRD: X-ray diffraction; NWs: nanowires; FTO: fluorine-doped tin oxide.

$\epsilon < 0.2\%$ for all samples, strain is not expected to have a relevant effect on the physical properties of the photoanodes^[67–69].

The cell parameters obtained for the hematite structure by the Rietveld Refinement, and the calculated unit cell volume V are shown in Table 1. It is observed that the undoped sample subjected to a two-step annealing process presents a slightly larger unit cell than the sample subjected to a one-step annealing process. However, this difference is minimal and could be attributed to the incorporation of Sn⁴⁺, which has an ionic radius of 0.69 Å, slightly larger than that of Fe³⁺, at 0.65 Å, within the structure^[70]. In the case of the Ti-doped samples, while the unit cell volume for the sample subjected to a single-step annealing process is comparable to that of the undoped sample, a significantly greater reduction in unit cell volume is observed when the annealing occurs at 800 °C. This is likely due to the incorporation of Ti⁴⁺, which has an ionic radius of 0.61 Å, smaller than that of Fe³⁺, and suggests that the higher temperature of 800 °C facilitates a more effective integration of Ti into the α -Fe₂O₃ structure compared to the 600 °C annealing process^[70].

Supplementary Figure 2 shows the Raman spectra of different synthesized photoanodes. The spectra are consistent with the α -Fe₂O₃ structure, with the peaks at 244 cm⁻¹, 293 cm⁻¹, 410 cm⁻¹ and 612 cm⁻¹ corresponding to doubly degenerate E_g modes and those at 225 cm⁻¹ and 497 cm⁻¹ to single degenerate A_{1g} modes^[71–73]. The full width at half maximum (FWHM) of each peak is shown in Supplementary Table 2. A greater broadening of the peaks is observed for the Ti-doped samples. This is consistent with the smaller crystallite size observed for the Ti-doped samples in relation to the undoped ones.

Table 1. Cell parameters obtained from the Rietveld Refinement for each of the samples. The unit cell volume is also shown

Sample	600PA	Ti600PA	800PA	Ti800PA
<i>a</i> (Å)	5.0299	5.0295	5.0322	5.0174
<i>c</i> (Å)	13.7335	13.7467	13.7339	13.7085
Volume (Å ³)	300.9	301.1	301.2	298.9

Surface composition

To assess the surface composition, an XPS study was performed on the 800PA, Ti600PA and Ti800PA photoanodes. The full survey for each sample and the high-resolution spectra corresponding to Fe 2p, O 1s, Sn 3d and Ti 2p are shown in Figure 3. For high-resolution spectra, the background was considered by applying a Shirley baseline model^[74].

In the full survey spectra, shown in Figure 3A, it is observed that the most intense signals correspond to the characteristic Fe and O peaks of hematite. Also, presence of Sn coming from the diffusion from the FTO substrate can be observed, along with Ti, for the samples doped with this element. In addition, a significant amount of C is observed, mainly due to adventitious carbon contamination during air exposure. In addition, traces of Si are observed at a very low concentration, probably due to small impurities introduced by the glass substrate itself. Also, a very small signal associated with N is appreciated, probably due to traces of the precursors.

The spectral region associated with the Fe 2p photoemission peak is shown in Figure 3B. Two split spin-orbit components are observed, located at 710.4-710.7 eV (Fe 2p_{3/2}) and at 723.8-724.1 eV (Fe 2p_{1/2}), which are consistent with the reported BE in α -Fe₂O₃^[75-77]. Furthermore, the separation in energy of the two spin orbital components is 13.4-13.5 eV, which clearly verifies the formation of Fe₂O₃^[71]. No significant shift was observed between the different samples, and the small difference between the position of the different peaks could be due to small calibration errors of the analyzer, since it has been reported that using adventitious carbon for charge referencing can induce an error of the order of 0.25 eV in the position of the rest of the peaks^[78]. In addition, surface components, associated with a higher BE, have been observed for both Fe 2p_{1/2} and Fe 2p_{3/2} photoemission peaks. These structures present BE of ~713 eV and ~726 eV, respectively. These surface peaks may indicate an atomic disorder on the surface of the material, which leads to a low electron density around the Fe(III) atoms. Consequently, the energy required to produce photoelectrons from these atoms is greater^[79]. The atomic percentage of Fe corresponding to the surface component is approximately 38%, 41% and 43% for the 800PA, Ti600PA and Ti800PA samples, respectively. Therefore, no significant dependence is observed on the annealing temperature, or on the doping with Ti. Also, an additional very broad peak is observed at an energy of 717-719 eV, corresponding with the shake - up satellite associated with the Fe 2p_{3/2} photoemission peak from α -Fe₂O₃^[80,81].

The O 1s spectral region is shown in Figure 3C. This region has been fitted with three Gaussian - Lorentzian peaks corresponding to lattice oxygen at the lowest BE (mainly Fe-O), to defective surface oxides or surface hydroxides at the medium BE, and to absorbed water or organic O at the highest BE^[82,83]. The Fe-O peak is located at 529.6-529.9 eV, which is consistent with the reported BE in α -Fe₂O₃^[39,84]. It is also worth mentioning that the percentage of the oxygen that forms the Fe-O bond, and the total oxygen is 51 %, 37 % and 23 % for the 800PA, Ti600PA and Ti800PA samples, respectively. Since the XPS measurements were performed after the PEC study, these differences may simply be due to small variations in the amount of -OH groups that have remained adhered to the surface, or to water or organic solvent molecules that may have been absorbed in the sample after the cleaning process.

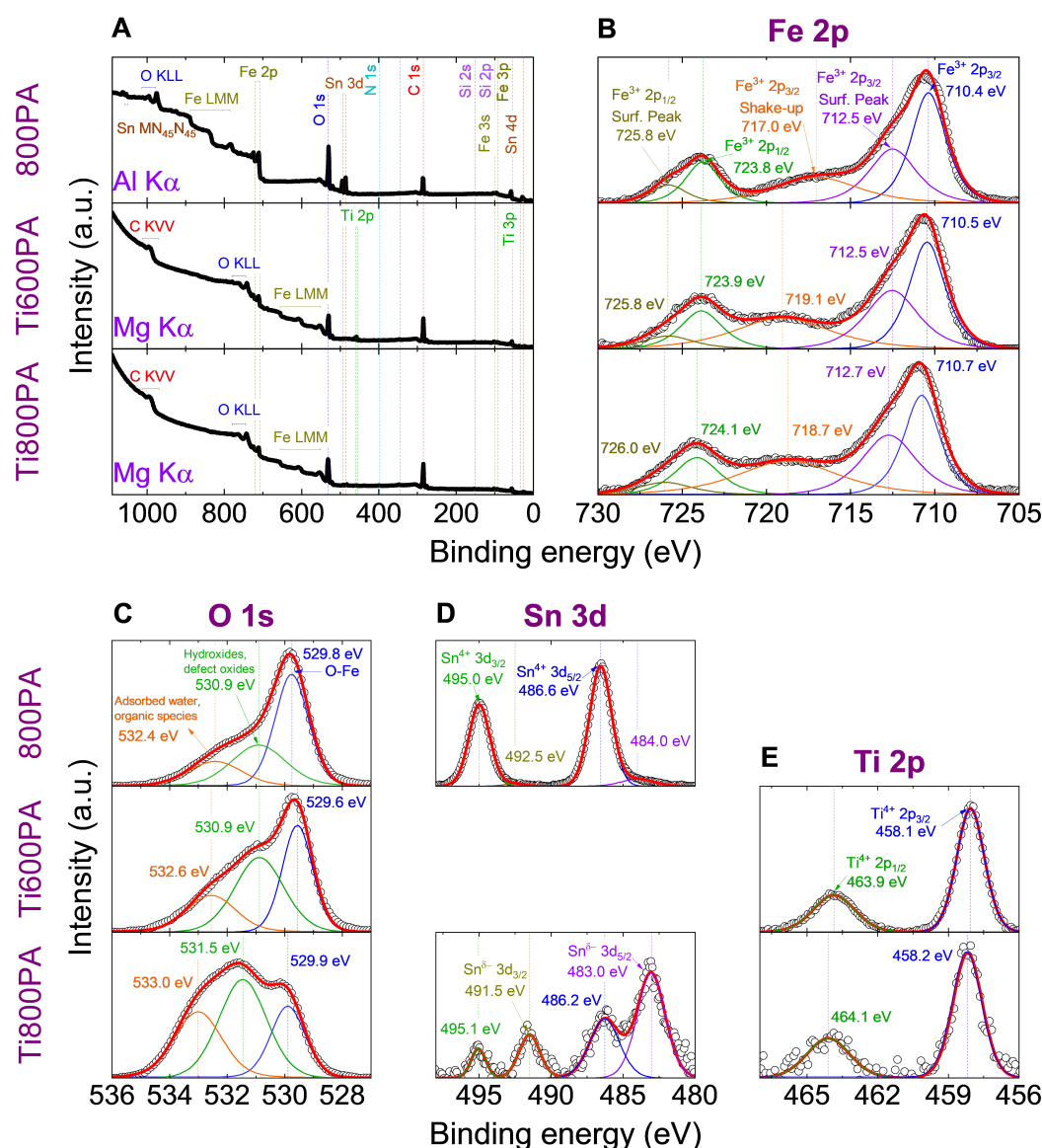


Figure 3. XPS spectra collected from the 800PA, Ti600PA and Ti800PA photoanodes: (A) full survey; (B) Fe 2p; (C) O 1s; (D) Sn 3d; (E) Ti 2p. For high-resolution spectra, the background was deduced by applying a Shirley baseline model. XPS: X-ray photoelectron spectroscopy.

In Figure 3D, the spectral region corresponding to Sn 3d is shown. For the 800PA, two peaks at ~486.6 eV and ~495.0 eV are observed, corresponding to the photoemission peaks associated with the 3d_{5/2} and 3d_{3/2} levels of Sn, respectively, which are consistent with the Sn⁴⁺ oxidation state^[85,86]. Additionally, two weak peaks are observed at lower BE than the previous ones. The BE of these peaks is significantly lower than that expected for metallic tin (485.0 eV for the 3d_{5/2} peak)^[87], so they must be negatively charged Sn species. Similar effects have been reported by other authors^[88,89]. For the 800PA sample, more than 93% of the Sn is in the Sn⁴⁺ state; in the case of the Ti800PA sample, this percentage is reduced to 36%, with the remaining 64% corresponding to negatively charged Sn species. In both cases, no metallic Sn is observed. The origin of these negatively charged species may be due to the incorporation of some Sn ions into the hematite structure, replacing O, or to the formation of some SnNa_x species on the surface during PEC measurements. In this case, Na may not be observed in the survey spectrum because its sensitivity factor is four times lower

than that of Sn, whose concentration is already low. For the Ti600PA sample, the amount of Sn on the surface is lower than the detection limit of the technique, suggesting a barrier effect of the Ti doping, which prevents Sn diffusion towards the photoanode surface.

Finally, [Figure 3E](#) shows the spectral region corresponding to Ti 2p, for the Ti-doped samples. In both cases, two peaks at ~ 458.1 eV and ~ 464.0 eV are observed, corresponding to the photoemission peaks associated with Ti levels $2p_{3/2}$ and $2p_{1/2}$, respectively. For titanium (IV) oxide, the position of the $2p_{3/2}$ peak would be expected to be located at ~ 458.7 eV. This shift to lower BE has also been reported by other authors for Ti-doped hematite^[41,59,90-93]. This suggests that the Ti atoms are in a different chemical environment compared to the TiO_2 structure, confirming their incorporation into the $\alpha\text{-Fe}_2\text{O}_3$ crystal structure^[59,93]. Also, in both cases, there is a separation of 5.8-5.9 eV between the $2p_{3/2}$ and $2p_{1/2}$ peaks, which confirms that the titanium is in Ti^{4+} state.

A quantitative estimation of the surface composition has been performed based on the intensity of the signals associated with each element. For this, the sensitivity factors provided by the manufacturer of the analyzer have been considered. When conducting this calculation, the carbon and oxygen that do not form Fe-O bonds have not been considered, since they are essentially surface features present on the outfacing side of the sample. Thus, [Table 2](#) shows the relative concentration of $\text{O}_{\text{lattice}}$, Fe, Sn and Ti for each of the samples.

A higher concentration of Ti on the surface is observed for an annealing temperature of 600 °C (9.2 at.%) compared to 800 °C (1.4 at.%). Furthermore, it should be noted that for the two samples annealed at 800 °C, the Sn concentration in the undoped sample is about seven times higher than in the Ti-doped sample. This variation may be attributed to the more defined morphology and ordering of the NWs of the undoped sample. As a result, part of the analyzed area may correspond to an area with a very low hematite thickness, facilitating better diffusion of Sn towards the surface for this sample (no Ti barrier).

In-depth compositional characterization.

While XPS is a very useful technique to determine with great precision the composition and chemical state of the different elements present on the outmost (5-10 nm) of the sample, using Rutherford Backscattering Spectrometry (RBS) makes it possible to determine the in-depth distribution of the different elements present in the photoanodes^[94,95].

[Supplementary Figure 3](#) shows the RBS spectra obtained for the 800PA, Ti600PA and Ti800PA samples. Only the relevant part of the spectra, corresponding to the hematite photoanode and the FTO layer, is shown. To simulate the diffusion of Sn from the FTO substrate and the incorporation of Ti, the experimental data have been fitted, simulating up to twenty layers corresponding to hematite doped with different atomic percentages of Ti and Sn, on top of up to thirteen more layers containing Sn and O to simulate the FTO substrate. C was also considered when performing the simulations to consider possible organic contamination present in the samples.

According to the highest energy edge of the Fe signal, located at $\sim 3,205$ keV for all the samples, the presence of this element on the surface is identified. Furthermore, for the Ti-doped samples, the presence of Ti on the surface is also observed in both samples, as per its high energy edge, located at $\sim 3,056$ keV. The lower energy edges of the Fe and Ti signal, along with the high energy edge of the Sn signal, are quite smooth. This effect is particularly prominent in the undoped sample annealed at 800 °C. This phenomenon results from a combination of Sn diffusion from the FTO substrate towards the surface, and the more defined morphology

Table 2. Surface composition of the different samples estimated by XPS

Sample	800C	Ti600PA	Ti800PA
O _{lattice} (at.%)	62.4	65.3	62.7
Fe (at.%)	28.3	25.5	35.5
Sn (at.%)	8.3	<LoD	1.2
Ti (at.%)	--	9.2	1.4

XPS: X-ray photoelectron spectroscopy; LoD: limit of detection.

and ordering of the NWs for the undoped samples. Consequently, not all the incident ions pass through the same amount of hematite, leading to non-uniform energy loss among the ions that reach the FTO layer.

Figure 4 shows the depth concentration profile of Fe, Ti, and Sn and the variation of the [Sn]/[Fe] and [Ti]/[Fe] ratios with depth. It is observed that the Sn concentration is much higher on surface in the undoped sample than in the doped ones, which is consistent with the more defined morphology and ordering of the NWs for the undoped samples observed by SEM. This can lead to the hematite thickness being very low in certain parts of the sample, favoring the diffusion of a greater number of Sn atoms to the surface. Also, no significant difference is observed in the Sn concentration profile for the two annealing conditions applied to Ti-doped samples.

In relation to the Ti concentration, it is observed that, although in both cases the [Ti]/[Fe] ratio is greater in the most superficial part of the sample than in bulk, the difference is greater for the 600 °C annealed sample. This is consistent with the results observed by XPS. However, the difference in Ti concentration between the two samples is small compared to the results obtained by XPS. This may be due to the surface sensitivity of XPS, which analyzes only the first 5-10 nm of the sample. In contrast, while RBS can estimate a depth profile, it is not the appropriate technique to resolve the exact concentration of the most superficial part. Additionally, Ti analysis by RBS is challenging due to its low concentration, low Rutherford cross-section compared with Fe and Sn and the partial overlap of its characteristic structure with that of Fe. Therefore, while the results provide an approximate idea of the depth distribution of the different elements in the samples, the distribution of Ti presents a higher uncertainty than for Fe and Sn.

Regarding the bulk Ti concentration, it is higher for the 800 °C annealed sample. This suggests that the nucleation and growth of FeO(OH) NWs occurs in the first stage of the synthesis process, with Ti being incorporated later, mostly on the surface. Through thermal annealing processes, the diffusion of Ti throughout the Fe₂O₃ matrix is favored. The higher the temperature, the greater this effect is confirmed to be.

By considering the atomic thickness of each layer used in the model and the percentage of Fe in each simulated layer, it is possible to estimate the total atomic thickness of the hematite layer, measured in Fe atoms/cm², for each sample. This is shown in Figure 5, along with the thickness measured by SEM. For the undoped sample annealed at 800 °C, the atomic thickness is approximately 6.4×10^{17} Fe atoms/cm². For the doped samples, the atomic thickness is 4.7×10^{17} Fe atoms/cm² and 4.9×10^{17} Fe atoms/cm² for the one-step and two-step annealing samples, respectively. This indicates that Ti doping reduces the total amount of Fe atoms in the sample by 20%-30%. However, the thickness measured by SEM for the Ti-doped samples is slightly higher than for the undoped samples. This suggests that the volume occupied by voids inside the doped samples is higher than in the case of the undoped samples, probably leading to a larger porosity for the Ti-doped photoanodes. Additionally, the fact that the two doped samples present a similar amount of Fe

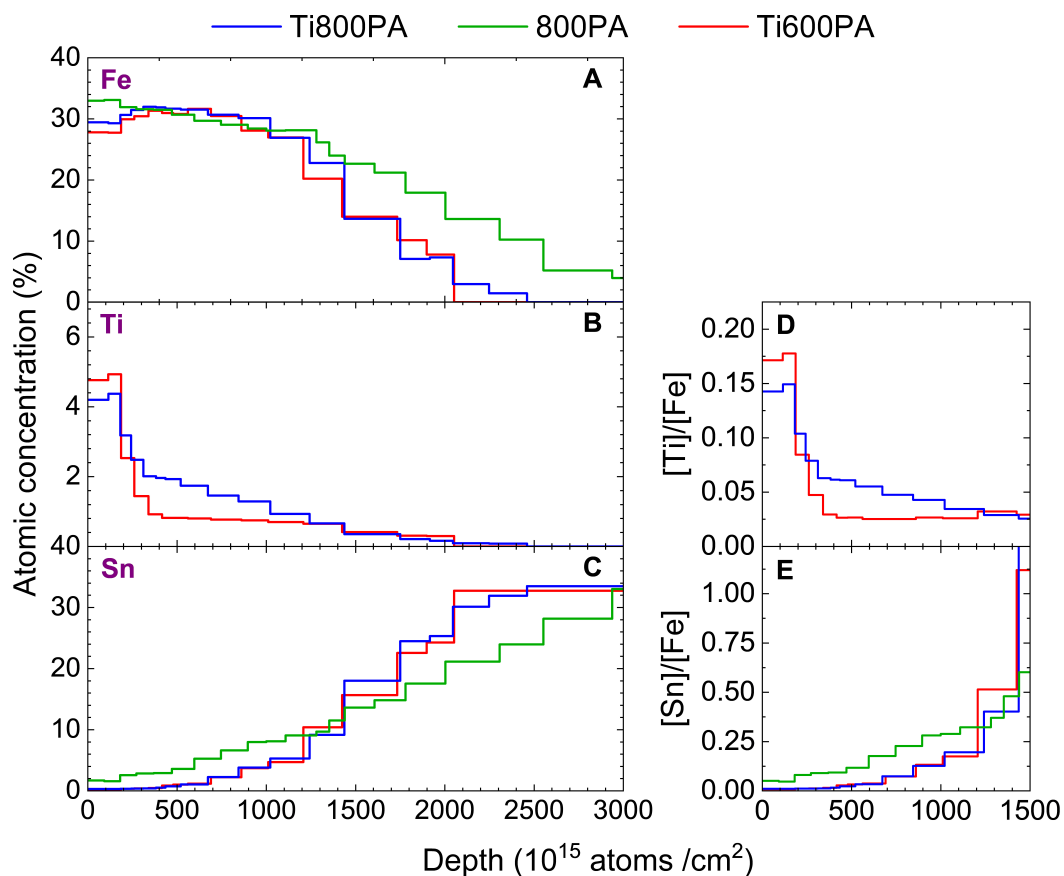


Figure 4. In-depth concentration profiles of (A) Fe; (B) Ti and (C) Sn obtained from the analysis of the RBS spectra, for the 800PA, Ti600PA and Ti800PA samples; (D) [Ti]/[Fe] ratio, and (E) [Sn]/[Fe] ratio depth profiles. RBS: Rutherford backscattering spectrometry.

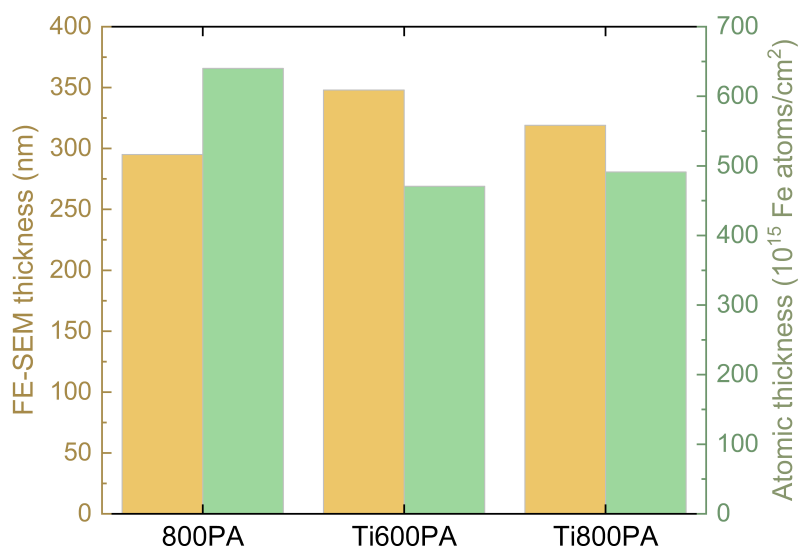


Figure 5. Nanometric thickness, measured by FE-SEM, and atomic thickness, measured by RBS for the 800PA, Ti600PA and Ti800PA samples. FE-SEM: Field emission scanning electron microscopy; RBS: Rutherford backscattering spectrometry.

atoms is expected since, although the distribution of these in the sample could change during the annealing processes, their incorporation is necessarily done during the hydrothermal synthesis process.

PEIS characterization

Figure 6A shows the Nyquist plot of the Ti600PA, 800PA and Ti800PA photoanodes. Likewise, Figure 6B shows a schematic representation of the equivalent circuit used to fit the experimental data. The circuit consists of the following elements: (1) A series resistance R_{Series} corresponding mainly to the small resistance of the FTO substrate; (2) A resistance R_{Bulk} associated with the recombination of electron-hole pairs in bulk, in parallel with a capacitance C_{Bulk} associated with charge accumulation in bulk; (3) A resistance $R_{CT,SS}$ corresponding to the charge transfer resistance from the surface states to the electrolyte, in parallel with its corresponding capacitance C_{SS} ^[9,96]. Capacitors were modeled as constant phase elements (CPEs), to consider the possibility of non-uniform current distribution^[51].

Table 3 shows the values of the different elements of the equivalent circuit, for the three samples analyzed. It is observed how the R_{Series} is similar and small in all cases, of about $R_{Series} \sim 30\text{--}60\ \Omega$. Concerning the resistance associated with the recombination of electron-hole pairs in bulk, it is minimal for the Ti800PA sample, obtaining a value of $134\ \Omega$, higher for the 800PA sample ($516\ \Omega$), and maximum for the Ti600PA sample ($1,111\ \Omega$). This indicates that both Ti doping and high-temperature annealing contribute to the reduction of the recombination of electron-hole pairs in bulk. The reduction of R_{bulk} with Ti doping is consistent with the incorporation of Ti^{4+} cations into the $\alpha\text{-Fe}_2\text{O}_3$ structure^[38,59]. Also, the reduction of R_{bulk} with increasing annealing temperature is consistent with the increase in crystallinity observed for the $800\ ^\circ\text{C}$ annealed samples, which contributes to the reduction of non-radiative recombination at grain boundaries^[97–100], as well as to the incorporation of Sn^{4+} cations at the interface with the FTO substrate when annealing at $800\ ^\circ\text{C}$ ^[11,101]. The higher conductivity of the semiconductor implies a better quantum efficiency of the photoanodes due to the fewer photogenerated electron-hole pairs that recombine^[102].

On the other hand, the resistance associated with the charge transfer between the surface states and the electrolyte $R_{CT,SS}$ is maximum for the 800PA sample ($4,080\ \Omega$), and lower for the Ti-doped samples ($1,590\ \Omega$ and $1,192\ \Omega$ for the Ti600PA and Ti800PA samples, respectively). This suggests that the presence of Ti^{4+} ions at the surface prevents positive charge accumulation at the hematite surface and decreases the surface recombination of the trapped electrons with holes from the valence band, favoring an increment of the quantum efficiency of the system.

Photoelectrochemical performance

Figure 7A shows the current J - V characteristics for the synthesized $\alpha\text{-Fe}_2\text{O}_3$ photoanodes in the dark and under simulated sunlight. For the undoped one-step annealed sample, J is very low, $\sim 0.02\ \text{mA}\cdot\text{cm}^{-2}$ (at $1.45\ \text{V}_{\text{RHE}}$), attributed to the low conductivity and short hole diffusion length in the obtained $\alpha\text{-Fe}_2\text{O}_3$ ^[6,8,11]. The incorporation of Ti dopant allowed a J increase to $0.64\ \text{mA}\cdot\text{cm}^{-2}$ (at $1.45\ \text{V}_{\text{RHE}}$), about 30 times higher than that of the undoped sample. With the two-step annealing scheme, a J improvement ($0.85\ \text{mA}\cdot\text{cm}^{-2}$ at $1.45\ \text{V}_{\text{RHE}}$) was observed for the undoped sample, while a J value of $1.27\ \text{mA}\cdot\text{cm}^{-2}$ (at $1.45\ \text{V}_{\text{RHE}}$) was obtained for the Ti-doped sample.

The improvement of J under sunlight illumination for the Ti-doped samples, compared to the undoped ones, is mainly due to the presence of Ti^{4+} ions on the surface, which prevent the accumulation of positive charges. Therefore, there is a decrease in the surface recombination of trapped electrons with holes in the valence band, as shown by PEIS measurements. This favors the quantum efficiency of the photoanodes. Furthermore, the reduction in bulk resistance observed, due to the presence of Ti^{4+} ions, also contributes to improving the quantum efficiency of the photoanodes.

Table 3. Value of each element of the considered equivalent circuit, for the Ti600PA, 800PA and Ti800PA photoanodes

Sample	Ti600PA	800PA	Ti800PA
R_{Series} (Ω)	37	52	49
R_{Bulk} (Ω)	1111	516	134
C_{Bulk} (μF)	4.1	4.3	5.0
$R_{CT,SS}$ (Ω)	1590	4080	1192
C_{SS} (μF)	7.8	24.4	5.8

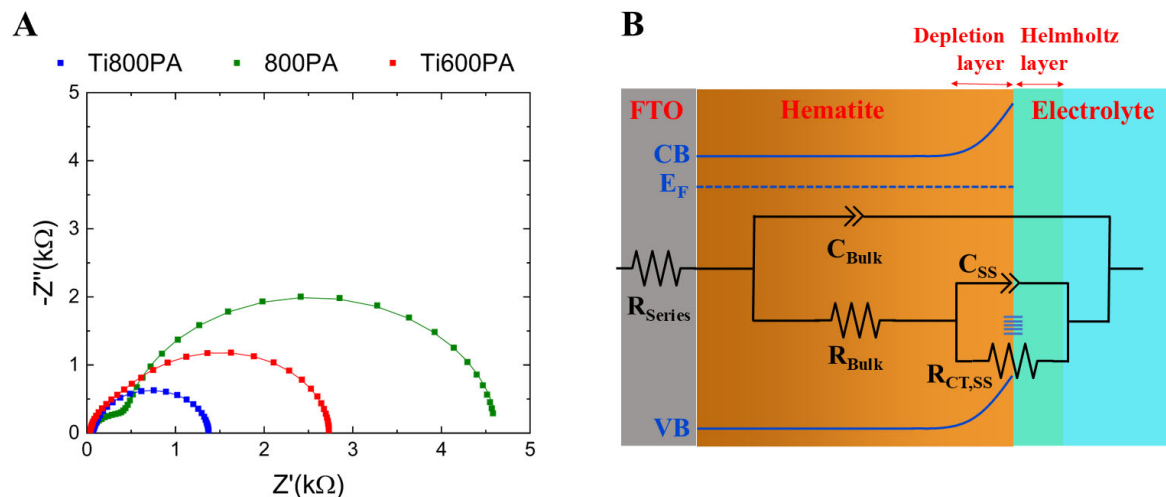


Figure 6. (A) Nyquist impedance plots of the Ti600PA, 800PA and Ti800PA photoanodes obtained under illumination and $V_{RHE} = 1$ V; (B) Equivalent electrical circuit used to fit the impedance data under illumination.

On the other hand, the improvement of J for the samples subjected to a two-step annealing scheme, compared to the one-step annealed samples, is essentially due to a decrease in bulk recombination, as observed by PEIS measurements. This is associated, on the one hand, with an increase in crystallite size, observed by XRD, as well as with the possible incorporation of Sn^{4+} cations at the interface with the FTO substrate when annealing at 800 °C. Furthermore, the greater preferential orientation in the (110) direction of these samples also favors a greater photocurrent, since the conductivity in the [110] direction is much higher than in directions orthogonal to it^[61,62]. However, despite the improvement in the photocurrent with Ti and Sn co-doping, the photocurrent value obtained is not yet comparable to reported values of up to ~ 6 mA/cm²^[103-106].

However, while for the undoped 800 °C annealed sample, the onset potential is ~ 0.90 V_{RHE}, an anodic shift in the onset potential is observed for the Ti-doped samples (~ 0.93 V_{RHE} and ~ 0.97 V_{RHE} for the 800 °C and 600 °C annealed samples, respectively). This is possibly due to the additional donor levels introduced by surface doping with Ti, which affects band bending at the semiconductor-electrolyte interface^[107]. Theoretical research by Toroker also indicated that a much larger overpotential was needed for water oxidation when hematite was doped with Ti on the surface^[108]. Additionally, the Ti-doped samples present a step photocurrent rise. This has been reported to be associated with a reduction in recombination in surface states^[109], consistent with what was observed by PEIS.

No significant variation of J_{dark} is observed when the photoanodes are doped with Ti. However, a notable decrease in J_{dark} is observed when the samples are subjected to the two-step annealing treatment, compared

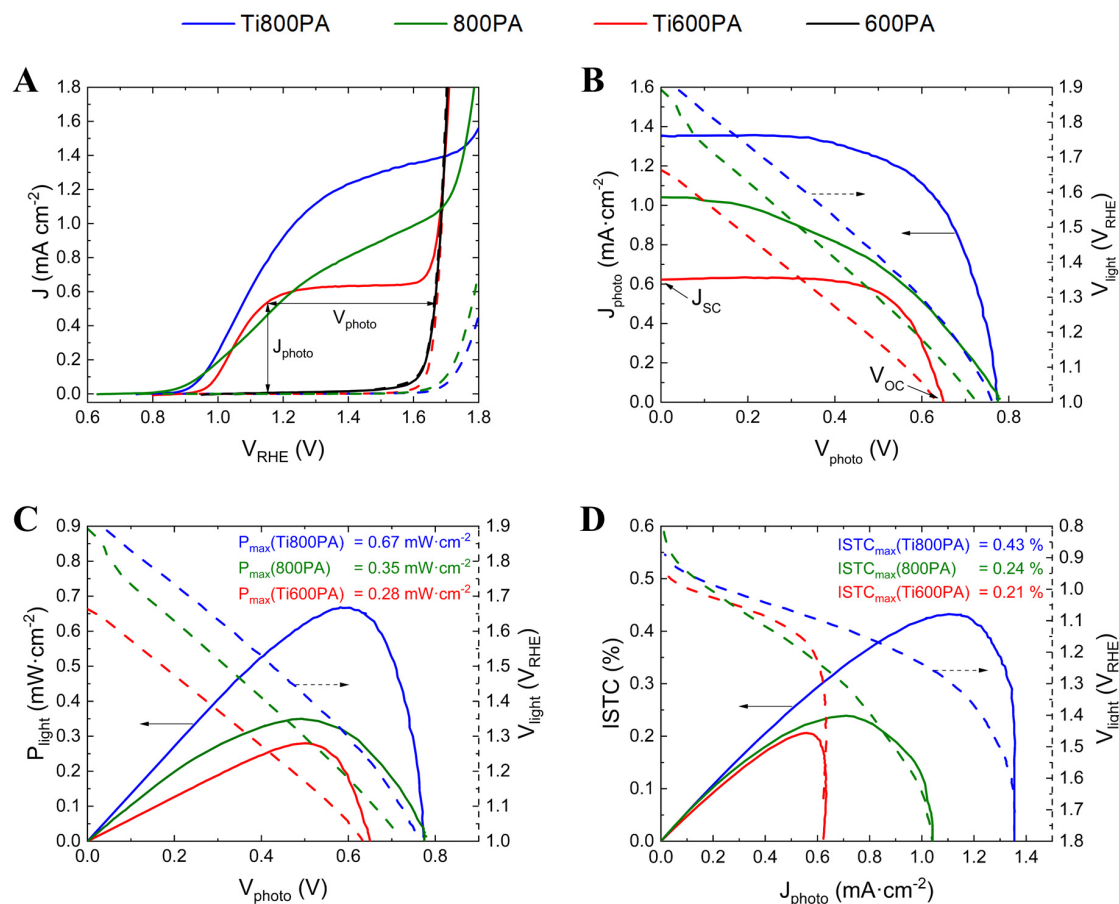


Figure 7. (A) J - V curves for the 600PA, Ti600PA, 800PA, Ti800PA photoanodes, obtained under simulated solar illumination (solid lines), and in the dark (dashed lines); (B) J_{photo} as a function of V_{photo} ; (C) Intrinsic photovoltaic power P_{light} as a function of V_{photo} ; (D) ISTC efficiency as a function of J_{photo} . For (b-d), the potential V_{light} applied to the photoanode under simulated solar illumination to obtain each V_{photo}/J_{photo} value is shown with dashed lines. J - V : Photocurrent density-voltage; ISTC: intrinsic solar-to-chemical.

to when they are subjected to the one-step annealing treatment, consistent with previous studies^[9,12].

The photocurrent J_{photo} and photopotential V_{photo} were extracted from the J - V curves, as shown in Figure 7A. J_{photo} was plotted as a function of V_{photo} , so that the photocurrent density measured under short-circuit conditions J_{SC} and the open-circuit photopotential V_{OC} can be determined, as shown in Figure 7B. A J_{SC} value of 1.35 mA cm⁻², 1.04 mA cm⁻² and 0.63 mA cm⁻² was obtained for the Ti800PA, 800PA and Ti600PA photoanodes, respectively, consistently with the better PEC performance of the Ti-doped samples with two-step annealing. Also, a V_{OC} value of 0.77 V, 0.77 V and 0.65 V, was obtained for the Ti800PA, 800PA and Ti600PA samples, respectively.

The intrinsic photovoltaic power P_{light} of the photoanodes as a function of V_{photo} is shown in Figure 7C. This way, the conditions for working at the MPP can be determined. For the Ti600PA and the 800PA photoanodes, maximum powers of 0.28 mW cm⁻² (at $V_{light} = 1.17 V_{RHE}$) and 0.35 mW cm⁻² (at $V_{light} = 1.31 V_{RHE}$) were obtained, respectively. For the Ti800PA sample, the maximum power increases substantially, obtaining a value of 0.67 mW cm⁻² (at $V_{light} = 1.29 V_{RHE}$). This confirms the pertinence of combining Ti doping and high-temperature annealing processes to notably improve the efficiency of the PEC cell. The photocurrent J_{MPP} at the MPP was 0.56 mA cm⁻², 0.71 mA cm⁻², and 1.11 mA cm⁻² for the

Ti600PA, 800PA and Ti800PA photoanodes, respectively, while the photovoltage V_{MPP} at the *MPP* was 0.50 V, 0.49 V and 0.60 V, respectively. The *MPP* determines the optimal condition for operating the PEC cell.

The *FF* at the *MPP* was calculated for each photoanode applying eq. (3). For the Ti-doped samples, a *FF* at *MPP* of 64 % and 68 % was obtained for the photoanodes subjected to two-step and one-step annealing processes, respectively. This value is much higher than the one obtained for the undoped 800 °C annealed sample (*FF* at *MPP* of 44 %). Previous works have reported that the greater the *FF*, the greater the charge extraction compared to the recombination of electron-hole pairs^[110,111]. Therefore, the fact that the Ti-doped samples present a higher *FF* indicates that charge extraction is favored by Ti-doping, consistent with the reduction of $R_{CT,SS}$ observed by PEIS, which is associated with a reduction of the positive charge accumulation at the hematite surface.

To evaluate the efficiency of the Ti-doped photoanodes in the conversion of solar into chemical energy necessary for water splitting, the *ISTC* conversion efficiency was determined by applying eq. (1). Figure 7D shows the plot of *ISTC* efficiency as a function of J_{photo} . *ISTC* maximum efficiencies of 0.21 % (at $J_{MPP} = 0.56 \text{ mA}\cdot\text{cm}^{-2}$), 0.25 % (at $J_{MPP} = 0.71 \text{ mA}\cdot\text{cm}^{-2}$) and 0.43 % (at $J_{MPP} = 1.11 \text{ mA}\cdot\text{cm}^{-2}$) were obtained for the Ti600PA, 800PA and Ti800PA photoanodes, respectively. To obtain the same dark current values, it would be necessary to apply potentials of 1.67 V_{RHE} , 1.80 V_{RHE} and 1.87 V_{RHE} , respectively, for the Ti600PA, 800PA and Ti800PA samples. Consequently, a simulated solar light of 0.28 $\text{mW}\cdot\text{cm}^{-2}$, 0.35 $\text{mW}\cdot\text{cm}^{-2}$ and 0.64 $\text{mW}\cdot\text{cm}^{-2}$ for the Ti600PA, 800PA and Ti800PA photoanodes is saved.

A stability test was performed using the one-step annealed Ti-doped $\alpha\text{-Fe}_2\text{O}_3$ sample [Figure 8]. J remained stable during a continuous measurement over 2 h applying a bias potential of 1.23 V_{RHE} under simulated 1-sun, showing a mean value of $0.570 \pm 0.003 \text{ mA}\cdot\text{cm}^{-2}$. These results confirm the good stability properties of hematite, without signs of photocorrosion^[5,112–115].

To better understand the higher photocurrent obtained for Ti-doped photoanodes, *IPCE* measurements at $V_{RHE} = 1.45 \text{ V}$ were performed as a function of the wavelength of the incident light, as shown in Figure 9. As can be seen, the Ti800PA sample presents the highest *IPCE* at all wavelengths, with a maximum of 34%, while the 800PA and Ti600PA samples present maximum values of 23% and 17%, respectively. These results indicate a positive effect of Sn and Ti co-doping on water oxidation photoactivity. Interestingly, the Ti-doped samples exhibit a slight shoulder at approximately 370 nm. This is relevant because at wavelength values in this range the solar spectral irradiance starts to grow remarkably, so the improvement of the *IPCE* in this range contributes significantly to the enhancement of the photocurrent.

CONCLUSIONS

Ti-doped hematite NWs were synthesized via hydrothermal synthesis, and the impact of applying a high-temperature annealing process to the photoanodes was investigated. Doping with Ti led to a notable increase in photocurrent under simulated solar illumination, rising from $0.02 \text{ mA}\cdot\text{cm}^{-2}$ to $0.63 \text{ mA}\cdot\text{cm}^{-2}$ (at 1.45 V_{RHE}) for the samples annealed at 600 °C, representing a 30-fold increase. This enhancement is attributed mainly to the passivation of surface states on hematite and an improvement in bulk conductivity. Additionally, when annealing was performed at 800 °C, the photocurrent increased to $0.87 \text{ mA}\cdot\text{cm}^{-2}$ and $1.27 \text{ mA}\cdot\text{cm}^{-2}$ (at 1.45 V_{RHE}) for the undoped and Ti-doped samples, respectively. The augmented photocurrent observed in samples subjected to high-temperature annealing is predominantly linked to the enhancement in bulk conductivity facilitated by the incorporation of Sn^{4+} ions in hematite and increased crystallinity. Notably, the Ti-doped, high-temperature annealed sample exhibited the highest photocurrent,

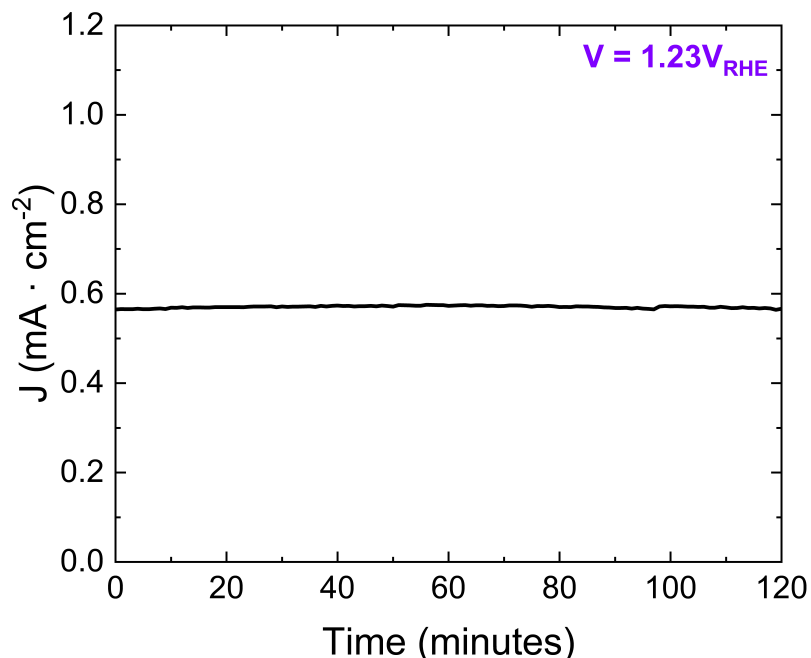


Figure 8. Photocurrent stability test for the Ti600 sample performed at 1.23 V_{RHE} for 2 h.

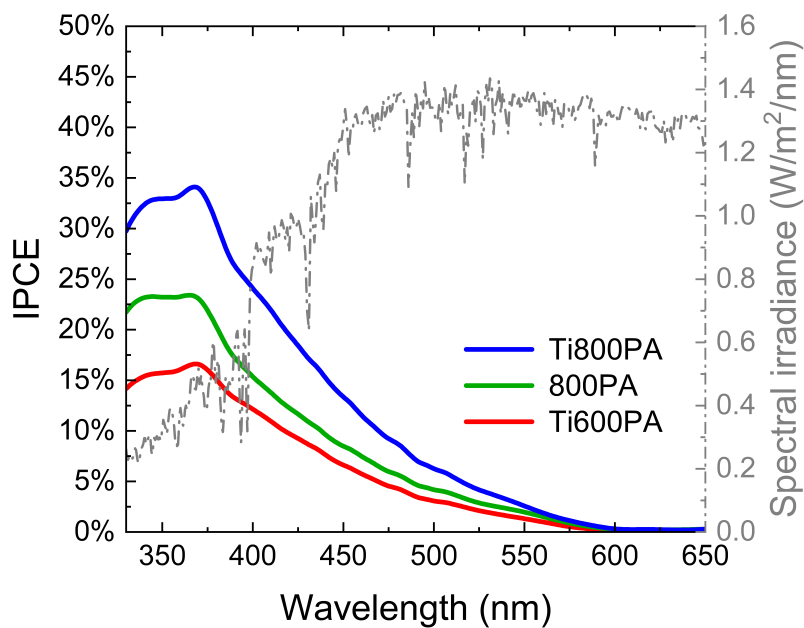


Figure 9. IPCE for the 800PA, Ti600PA and Ti800PA samples, at $V_{RHE} = 1.45$ V. In grey dashed lines, the solar radiation spectrum AM1.5 is shown. IPCE: incident photon-to-current efficiency.

confirming the pertinence of simultaneously applying Ti doping and high-temperature annealing to improve the PEC efficiency of the hematite photoanodes. Future investigations could focus on optimizing the Ti concentration and annealing temperature to achieve the highest PEC efficiency.

By deepening our comprehension of the impact of heteroatom doping on the properties of hematite semiconductors, and the possibility of applying this together with high-temperature annealing processes, this study lays the ground for the design and enhancement of efficient materials with high specific surface areas for sustainable chemical energy conversion applications.

DECLARATIONS

Acknowledgments

The authors thank the “Centro de Microanálisis de Materiales” for the beam time with reference STD044/23.

Authors' contributions

Conceptualization: Araújo, J. P.; Apolinario, A.; de Sousa, C. T.

Data curation: Fernández-Alonso, F. J.; Quiterio, P.; Vilarinho, R.

Formal analysis: Fernández-Alonso, F. J.; Quiterio, P.; Vilarinho, R.; Manso-Silván, M.; Torres-Costa, V.; Apolinario, A.; de Sousa, C. T.

Funding acquisition: Araújo, J. P.; de Sousa, C. T.

Investigation: Fernández-Alonso, F. J.; Quiterio, P.; Vilarinho, R.; Manso-Silván, M.; Torres-Costa, V.; Apolinario, A.; de Sousa, C. T.

Methodology: Fernández-Alonso, F. J.; Quiterio, P.; Vilarinho, R.; Torres-Costa, V.; Apolinario, A.; de Sousa, C. T.

Project administration: Araújo, J. P.; de Sousa, C. T.

Resources: Mendes, A.; Manso-Silván, M.; Torres-Costa, V.; Apolinario, A.; de Sousa, C. T.

Supervision: Araújo, J. P.; Manso-Silván, M.; Torres-Costa, V.; Apolinario, A.; de Sousa, C. T.

Visualization: Fernández-Alonso, F. J.; Quiterio, P.; Vilarinho, R.

Writing - original draft: Fernández-Alonso, F. J.; Quiterio, P.; de Sousa, C. T.

Writing - review and editing: Fernández-Alonso, Manso-Silván, M.; Torres-Costa, V.; Apolinario, A.; de Sousa, C. T.

Availability of data and materials

The data are available upon request from the authors.

Financial support and sponsorship

This research was financially supported by the grants PID2022-141080OB-C22 and CNS2024-154729, funded by MCIN/AEI. Fernández-Alonso, F.J. acknowledges the Formación de Profesorado Universitario programme, ref. FPU22/04365. de Sousa, C. T. acknowledges the programme Atracción de Talento (CAM), ref. 2020-T1/IND-19889. Apolinário, A. acknowledges FCT- Fundação para a Ciência e a Tecnologia DL57/2016 (Ref. DL 57/2016/CP1454/CT0017; <https://doi.org/10.54499/DL57/2016/CP1454/CT0017>) projects H2FlexiPEC's (ref. 2022.07332.PTDC; (<http://doi.org/10.54499/2022.07332.PTDC>), 2024.00223.CERN; H2INNOVATE (NORTE-01-0145-FEDER-000076); Laboratório de Física para Materiais e Tecnologias Emergentes (LaPMET), Instituto de Física de Materiais Avançados, Nanotecnologia e Fotónica Universidade do Porto (IFIMUP)-UIDB/04968/2020 (<https://doi.org/10.54499/UIDB/04968/2020>); UIDP/04968/2020 (<https://doi.org/10.54499/UIDP/04968/2020>). This article is based upon work from COST Action NETPORE, CA20126, supported by COST (European Cooperation in Science and Technology).

Conflicts of interest

All authors declared that there are no conflicts of interest.

Ethical approval and consent to participate

Not applicable.

Consent for publication

Not applicable.

Copyright

© The Author(s) 2025.

REFERENCES

1. Jackson, R. B.; Saunio, M.; Bousquet, P.; et al. Increasing anthropogenic methane emissions arise equally from agricultural and fossil fuel sources. *Environ. Res. Lett.* **2020**, *15*, 071002. DOI
2. Sudhaik, A.; Parwaz, K. A. A.; Raizada, P.; et al. Strategies based review on near-infrared light-driven bismuth nanocomposites for environmental pollutants degradation. *Chemosphere* **2022**, *291*, 132781. DOI
3. Ullah, S.; Chishti, M. Z.; Majeed, M. T. The asymmetric effects of oil price changes on environmental pollution: evidence from the top ten carbon emitters. *Environ. Sci. Pollut. Res.* **2020**, *27*, 29623-35. DOI PubMed
4. Grätzel, M. Photoelectrochemical cells. *Nature* **2001**, *414*, 338-44. DOI PubMed
5. Dias, P.; Vilanova, A.; Lopes, T.; Andrade, L.; Mendes, A. Extremely stable bare hematite photoanode for solar water splitting. *Nano. Energy* **2016**, *23*, 70-9. DOI
6. Sivula, K.; Le, F. F.; Grätzel, M. Solar water splitting: progress using hematite ($\alpha\text{-Fe}_2\text{O}_3$) photoelectrodes. *ChemSusChem* **2011**, *4*, 432-49. DOI
7. Murphy, A.; Barnes, P.; Randeniya, L.; et al. Efficiency of solar water splitting using semiconductor electrodes. *Int. J. Hydrogen. Energy* **2006**, *31*, 1999-2017. DOI
8. Tamirat, A. G.; Rick, J.; Dubale, A. A.; Su, W. N.; Hwang, B. J. Using hematite for photoelectrochemical water splitting: a review of current progress and challenges. *Nanoscale. Horiz.* **2016**, *1*, 243-67. DOI PubMed
9. Dias, P.; Andrade, L.; Mendes, A. Hematite-based photoelectrode for solar water splitting with very high photovoltage. *Nano. Energy* **2017**, *38*, 218-31. DOI
10. Formal F, Tétrault N, Cornuz M, Moehl T, Grätzel M, Sivula K. Passivating surface states on water splitting hematite photoanodes with alumina overlayers. *Chem. Sci.* **2011**, *2*, 737-43. DOI
11. Ling, Y.; Wang, G.; Wheeler, D. A.; Zhang, J. Z.; Li, Y. Sn-doped hematite nanostructures for photoelectrochemical water splitting. *Nano. Lett.* **2011**, *11*, 2119-25. DOI
12. Quitério, P.; Apolinário, A.; Navas, D.; et al. Photoelectrochemical water splitting: thermal annealing challenges on hematite nanowires. *J. Phys. Chem. C* **2020**, *124*, 12897-911. DOI
13. Zandi, O.; Hamann, T. W. Enhanced water splitting efficiency through selective surface state removal. *J. Phys. Chem. Lett.* **2014**, *5*, 1522-6. DOI PubMed
14. Bassi, P. S.; Antony, R. P.; Boix, P. P.; Fang, Y.; Barber, J.; Wong, L. H. Crystalline $\text{Fe}_2\text{O}_3/\text{Fe}_2\text{TiO}_5$ heterojunction nanorods with efficient charge separation and hole injection as photoanode for solar water oxidation. *Nano. Energy* **2016**, *22*, 310-8. DOI
15. Zhou, D.; Fan, K. Recent strategies to enhance the efficiency of hematite photoanodes in photoelectrochemical water splitting. *Chin. J. Catal.* **2021**, *42*, 904-19. DOI
16. Ni, S.; Wang, D.; Guo, F.; et al. Efficiency improvement of TiO_2 nanowire arrays based dye-sensitized solar cells through further enhancing the specific surface area. *J. Cryst. Growth* **2019**, *505*, 62-8. DOI
17. Dhara, A.; Show, B.; Baral, A.; et al. Core-shell CuO-ZnO p-n heterojunction with high specific surface area for enhanced photoelectrochemical (PEC) energy conversion. *Solar. Energy* **2016**, *136*, 327-32. DOI
18. Haider, Z.; Yim, H. W.; Lee, H. W.; Kim, H. Surface and bulk modification for advanced electrode design in photoelectrochemical water splitting. *Int. J. Hydrogen. Energy* **2020**, *45*, 5793-815. DOI
19. Park, J.; Kang, J.; Chaule, S.; Jang, J. Recent progress and perspectives on heteroatom doping of hematite photoanodes for photoelectrochemical water splitting. *J. Mater. Chem. A* **2023**, *11*, 24551-65. DOI
20. Dias, P.; Lopes, T.; Andrade, L.; Mendes, A. Temperature effect on water splitting using a Si-doped hematite photoanode. *J. Power. Sources* **2014**, *272*, 567-80. DOI
21. Niu, S.; Jiang, W. J.; Wei, Z.; et al. Se-doping activates FeOOH for cost-effective and efficient electrochemical water oxidation. *J. Am. Chem. Soc.* **2019**, *141*, 7005-13. DOI
22. Wang, J.; Xiang, Y.; Zhang, W.; et al. Integrating Cr doped FeOOH into FeSe_2 nanoparticles for efficient water oxidation at large current densities. *Fuel* **2023**, *351*, 128827. DOI
23. Lin, J.; Zhang, X.; Zhou, L.; Li, S.; Qin, G. Pt-doped $\alpha\text{-Fe}_2\text{O}_3$ photoanodes prepared by a magnetron sputtering method for photoelectrochemical water splitting. *Mater. Res. Bull.* **2017**, *91*, 214-9. DOI
24. Gurudayal; Chiam, S. Y.; Kumar, M. H.; et al. Improving the efficiency of hematite nanorods for photoelectrochemical water splitting by doping with manganese. *ACS. Appl. Mater. Interfaces* **2014**, *6*, 5852-9. DOI

25. Shen, S.; Jiang, J.; Guo, P.; Kronawitter, C. X.; Mao, S. S.; Guo, L. Effect of Cr doping on the photoelectrochemical performance of hematite nanorod photoanodes. *Nano. Energy*. **2012**, *1*, 732-41. DOI
26. Liu, J.; Cai, Y.; Tian, Z.; et al. Highly oriented Ge-doped hematite nanosheet arrays for photoelectrochemical water oxidation. *Nano. Energy*. **2014**, *9*, 282-90. DOI
27. Shen, S.; Kronawitter, C. X.; Jiang, J.; Mao, S. S.; Guo, L. Surface tuning for promoted charge transfer in hematite nanorod arrays as water-splitting photoanodes. *Nano. Res.* **2012**, *5*, 327-36. DOI
28. Zhang, M.; Luo, W.; Li, Z.; Yu, T.; Zou, Z. Surface modification of hematite photoanode films with rhodium. *Rare. Met.* **2011**, *30*, 38-41. DOI
29. Sivula, K.; Zboril, R.; Le, F. F.; et al. Photoelectrochemical water splitting with mesoporous hematite prepared by a solution-based colloidal approach. *J. Am. Chem. Soc.* **2010**, *132*, 7436-44. DOI
30. Cesar, I.; Sivula, K.; Kay, A.; Zboril, R.; Grätzel, M. Influence of feature size, film thickness, and silicon doping on the performance of nanostructured hematite photoanodes for solar water splitting. *J. Phys. Chem. C*. **2009**, *113*, 772-82. DOI
31. Malviya, K. D.; Dotan, H.; Shlenkevich, D.; Tsyganok, A.; Mor, H.; Rothschild, A. Systematic comparison of different dopants in thin film hematite (α -Fe₂O₃) photoanodes for solar water splitting. *J. Mater. Chem. A*. **2016**, *4*, 3091-9. DOI
32. Zhang, Y.; Ji, H.; Ma, W.; Chen, C.; Song, W.; Zhao, J. Doping-promoted solar water oxidation on hematite photoanodes. *Molecules* **2016**, *21*, 868. DOI PubMed PMC
33. Quang, N. D.; Van, P. C.; Le, D. D.; et al. Fluorine-surface-modified tin-doped hematite nanorod array photoelectrodes with enhanced water oxidation activity. *Appl. Surf. Sci.* **2021**, *558*, 149898. DOI
34. Quang N, Cao Van P, Majumder S, Jeong JR, Kim D, Kim C. Rational construction of S-doped FeOOH onto Fe₂O₃ nanorods for enhanced water oxidation. *J. Colloid. Interface. Sci.* **2022**, *616*, 749-58. DOI PubMed
35. Barroso, M.; Mesa, C. A.; Pendlebury, S. R.; et al. Dynamics of photogenerated holes in surface modified α -Fe₂O₃ photoanodes for solar water splitting. *Proc. Natl. Acad. Sci. U. S. A.* **2012**, *109*, 15640-5. DOI
36. Kim, J. H.; Kim, J. M.; Pan, Z.; Sohn, W. Y. Revealing the roles of surface treatments on hematite (α -Fe₂O₃) photoanode in the shift of the onset potential. *J. Photochem. Photobiol. A. Chem.* **2023**, *445*, 115037. DOI
37. Franking, R.; Li, L.; Lukowski, M. A.; et al. Facile post-growth doping of nanostructured hematite photoanodes for enhanced photoelectrochemical water oxidation. *Energy. Environ. Sci.* **2013**, *6*, 500-12. DOI
38. Pu, A.; Deng, J.; Li, M.; et al. Coupling Ti-doping and oxygen vacancies in hematite nanostructures for solar water oxidation with high efficiency. *J. Mater. Chem. A*. **2014**, *2*, 2491. DOI
39. Su, J.; Zhou, J.; Zong, S.; Zhou, Z.; Liu, C.; Feng, B. The effect of thermal annealing on the interfacial properties and photoelectrochemical performance of Ti doped Fe₂O₃ nanowire arrays. *RSC. Adv.* **2016**, *6*, 99851-8. DOI
40. Peng, Y.; Ruan, Q.; Lam, C. H.; et al. Plasma-implanted Ti-doped hematite photoanodes with enhanced photoelectrochemical water oxidation performance. *J. Alloys. Compd.* **2021**, *870*, 159376. DOI
41. Shen, S.; Kronawitter, C. X.; Wheeler, D. A.; et al. Physical and photoelectrochemical characterization of Ti-doped hematite photoanodes prepared by solution growth. *J. Mater. Chem. A*. **2013**, *1*, 14498. DOI
42. Zhang, P.; Kleiman-shwarstein, A.; Hu, Y.; et al. Oriented Ti doped hematite thin film as active photoanodes synthesized by facile APCVD. *Energy. Environ. Sci.* **2011**, *4*, 1020. DOI
43. Ling, Y.; Li, Y. Review of Sn-doped hematite nanostructures for photoelectrochemical water splitting. *Part. Part. Syst. Charact.* **2014**, *31*, 1113-21. DOI
44. Vayssieres, L.; Beermann, N.; Lindquist, S.; Hagfeldt, A. Controlled aqueous chemical growth of oriented three-dimensional crystalline nanorod arrays: application to iron(III) oxides. *Chem. Mater.* **2001**, *13*, 233-5. DOI
45. Francisco, F.; Dias, P.; Ivanou, D.; Santos, F.; Azevedo, J.; Mendes, A. Synthesis of Host-guest hematite photoelectrodes for solar water splitting. *ChemNanoMat* **2019**, *5*, 911-20. DOI
46. Yang, T.; Kang, H.; Jin, K.; et al. An iron oxide photoanode with hierarchical nanostructure for efficient water oxidation. *J. Mater. Chem. A*. **2014**, *2*, 2297-305. DOI
47. Schneider, C. A.; Rasband, W. S.; Eliceiri, K. W. NIH image to imageJ: 25 years of image analysis. *Nat. Methods*. **2012**, *9*, 671-5. DOI PubMed PMC
48. Seah, M. P.; Dench, W. A. Quantitative electron spectroscopy of surfaces: a standard data base for electron inelastic mean free paths in solids. *Surf. Interface. Anal.* **1979**, *1*, 2-11. DOI
49. Redondo-cubero, A.; Borge, M. J. G.; Gordillo, N.; et al. Current status and future developments of the ion beam facility at the centre of micro-analysis of materials in Madrid. *Eur. Phys. J. Plus.* **2021**, *136*, 1085. DOI
50. Mayer, M. SIMNRA, a simulation program for the analysis of NRA, RBS and ERDA. In: The fifteenth international conference on the application of accelerators in research and industry; Denton, Texas (USA): AIP; 1999. pp. 541-4. Available from: <https://pubs.aip.org/aip/acp/article/475/1/541-544/953322>. [Last accessed on 21 Mar 2025].
51. Lopes, T.; Andrade, L.; Le, F. F.; Gratzel, M.; Sivula, K.; Mendes, A. Hematite photoelectrodes for water splitting: evaluation of the role of film thickness by impedance spectroscopy. *Phys. Chem. Chem. Phys.* **2014**, *16*, 16515-23. DOI PubMed
52. Dare-edwards, M. P.; Goodenough, J. B.; Hamnett, A.; Trevellick, P. R. Electrochemistry and photoelectrochemistry of iron(III) oxide. *J. Chem. Soc., Faraday. Trans. 1.* **1983**, *79*, 2027. DOI
53. Ahn, H.; Kwak, M.; Lee, J.; Yoon, K.; Jang, J. Nanoporous hematite structures to overcome short diffusion lengths in water splitting. *J. Mater. Chem. A*. **2014**, *2*, 19999-20003. DOI

54. Dotan, H.; Mathews, N.; Hisatomi, T.; Grätzel, M.; Rothschild, A. On the solar to hydrogen conversion efficiency of photoelectrodes for water splitting. *J. Phys. Chem. Lett.* **2014**, *5*, 3330-4. DOI PubMed
55. Dotan, H.; Sivula, K.; Grätzel, M.; Rothschild, A.; Warren, S. C. Probing the photoelectrochemical properties of hematite ($\alpha\text{-Fe}_2\text{O}_3$) electrodes using hydrogen peroxide as a hole scavenger. *Energy. Environ. Sci.* **2011**, *4*, 958-64. DOI
56. Morrish, R.; Rahman, M.; MacElroy, J. M.; Wolden, C. A. Activation of hematite nanorod arrays for photoelectrochemical water splitting. *ChemSusChem* **2011**, *4*, 474-9. DOI PubMed
57. Zhao, X.; Feng, J.; Wang, N.; et al. The Influence of Ti doping on morphology and photoelectrochemical properties of hematite grown from aqueous solution for water splitting. *Energy. Tech.* **2018**, *6*, 2188-99. DOI
58. Mazzaro, R.; Boscolo, B. S.; Natali, M.; et al. Hematite nanostructures: an old material for a new story. Simultaneous photoelectrochemical oxidation of benzylamine and hydrogen production through Ti doping. *Nano. Energy.* **2019**, *61*, 36-46. DOI
59. Deng, J.; Zhong, J.; Pu, A.; et al. Ti-doped hematite nanostructures for solar water splitting with high efficiency. *J. Appl. Phys.* **2012**, *112*, 084312. DOI
60. Li, L.; Zhang, H.; Liu, C.; Liang, P.; Mitsuzaki, N.; Chen, Z. The effect of annealing regime and electrodeposition time on morphology and photoelectrochemical performance of hematite converted from nanosheet $\gamma\text{-FeOOH}$. *J. Photochem. Photobiol. A. Chem.* **2019**, *369*, 8-15. DOI
61. Kay, A.; Cesar, I.; Grätzel, M. New benchmark for water photooxidation by nanostructured $\alpha\text{-Fe}_2\text{O}_3$ films. *J. Am. Chem. Soc.* **2006**, *128*, 15714-21. DOI PubMed
62. Iordanova, N.; Dupuis, M.; Rosso, K. M. Charge transport in metal oxides: a theoretical study of hematite $\alpha\text{-Fe}_2\text{O}_3$. *J. Chem. Phys.* **2005**, *122*, 144305. DOI PubMed
63. Zhang, H.; He, Y.; Bao, X.; et al. Fabrication of hematite photoanode consisting of (110)-oriented single crystals. *ChemSusChem* **2023**, *16*, e202300666. DOI
64. Suryanarayana, C.; Norton, M. G. X-ray diffraction. 1th ed. Boston, MA: Springer US; 1998. Available from: <http://link.springer.com/10.1007/978-1-4899-0148-4>. [Last accessed on 21 Mar 2025].
65. Williamson, G.; Hall, W. X-ray line broadening from filed aluminium and wolfram. *Acta. Metall.* **1953**, *1*, 22-31. DOI
66. Maabong, K.; Machatine, A. G.; Mwankemwa, B. S.; et al. Nanostructured hematite thin films for photoelectrochemical water splitting. *Physica. B.* **2018**, *535*, 67-71. DOI
67. Apolinário, A.; Lopes, T.; Costa, C.; Araújo, J. P.; Mendes, A. M. Multilayered WO_3 nanoplatelets for efficient photoelectrochemical water splitting: the role of the annealing ramp. *ACS. Appl. Energy. Mater.* **2019**, *2*, 1040-50. DOI
68. Oliveira, G.; Machado, P.; Pires, A.; Pereira, A.; Araújo, J.; Lopes, A. Magnetocaloric effect and refrigerant capacity in polycrystalline YCrO_3 . *J. Phys. Chem. Solids.* **2016**, *91*, 182-8. DOI
69. Proenca, M. P.; Sousa, C. T.; Pereira, A. M.; et al. Size and surface effects on the magnetic properties of NiO nanoparticles. *Phys. Chem. Chem. Phys.* **2011**, *13*, 9561-7. DOI
70. Shannon, R. D. Revised effective ionic radii and systematic studies of interatomic distances in halides and chalcogenides. *Acta. Cryst. A.* **1976**, *32*, 751-67. DOI
71. Bhandary, N.; Singh, A. P.; Ingole, P. P.; Basu, S. Enhanced photoelectrochemical performance of electrodeposited hematite films decorated with nanostructured NiMnO_x . *RSC. Adv.* **2016**, *6*, 35239-47. DOI
72. Zhang, X.; Niu, Y.; Meng, X.; Li, Y.; Zhao, J. Structural evolution and characteristics of the phase transformations between $\alpha\text{-Fe}_2\text{O}_3$, Fe_3O_4 and $\gamma\text{-Fe}_2\text{O}_3$ nanoparticles under reducing and oxidizing atmospheres. *CrystEngComm* **2013**, *15*, 8166. DOI
73. Sarma, S. K.; Mohan, R.; Shukla, A. Structural, opto-electronic and photoelectrochemical properties of tin doped hematite nanoparticles for water splitting. *Mater. Sci. Semicond. Process.* **2020**, *108*, 104873. DOI
74. Shirley, D. A. High-resolution X-ray photoemission spectrum of the valence bands of gold. *Phys. Rev. B.* **1972**, *5*, 4709-14. DOI
75. Zhang, J.; Liu, X.; Wang, L.; et al. Synthesis and gas sensing properties of $\alpha\text{-Fe}_2\text{O}_3/\text{ZnO}$ core-shell nanospindles. *Nanotechnology* **2011**, *22*, 185501. DOI
76. Fu, Y.; Wang, R.; Xu, J.; et al. Synthesis of large arrays of aligned $\alpha\text{-Fe}_2\text{O}_3$ nanowires. *Chem. Phys. Lett.* **2003**, *379*, 373-9. DOI
77. Kang, M. J.; Yu, H.; Lee, W.; Cha, H. G. Efficient $\text{Fe}_2\text{O}_3/\text{C-g-C}_3\text{N}_4$ Z-scheme heterojunction photocatalyst prepared by facile one-step carbonizing process. *J. Phys. Chem. Solids.* **2019**, *130*, 93-9. DOI
78. Biesinger, M. C. Accessing the robustness of adventitious carbon for charge referencing (correction) purposes in XPS analysis: Insights from a multi-user facility data review. *Appl. Surf. Sci.* **2022**, *597*, 153681. DOI
79. Grosvenor, A. P.; Kobe, B. A.; Biesinger, M. C.; McIntyre, N. S. Investigation of multiplet splitting of Fe 2p XPS spectra and bonding in iron compounds. *Surf. Interface. Anal.* **2004**, *36*, 1564-74. DOI
80. Hao, S.; Wang, H.; Yang, R.; et al. Corn-like mesoporous $\text{SnO}_2/\alpha\text{-Fe}_2\text{O}_3$ heterostructure for superior TEA sensing performance. *Appl. Phys. A.* **2021**, *127*, 4350. DOI
81. Sun, L.; Wu, W.; Yang, S.; et al. Template and silica interlayer tailorable synthesis of spindle-like multilayer $\alpha\text{-Fe}_2\text{O}_3/\text{Ag}/\text{SnO}_2$ ternary hybrid architectures and their enhanced photocatalytic activity. *ACS. Appl. Mater. Interfaces.* **2014**, *6*, 1113-24. DOI
82. Biesinger, M. C.; Payne, B. P.; Grosvenor, A. P.; Lau, L. W.; Gerson, A. R.; Smart, R. S. Resolving surface chemical states in XPS analysis of first row transition metals, oxides and hydroxides: Cr, Mn, Fe, Co and Ni. *Appl. Surf. Sci.* **2011**, *257*, 2717-30. DOI
83. Payne, B.; Biesinger, M.; McIntyre, N. X-ray photoelectron spectroscopy studies of reactions on chromium metal and chromium oxide surfaces. *J. Electron. Spectrosc. Relat. Phenom.* **2011**, *184*, 29-37. DOI
84. Wang, L.; Nguyen, N. T.; Zhang, Y.; Bi, Y.; Schmuki, P. Enhanced solar water splitting by swift charge separation in Au/FeOOH

- sandwiched single-crystalline Fe₂O₃ nanoflake photoelectrodes. *ChemSusChem* **2017**, *10*, 2720-7. DOI
85. Tian, C. M.; Li, W.; Lin, Y. M.; et al. Electronic structure, optical properties, and photoelectrochemical activity of Sn-doped Fe₂O₃ thin films. *J. Phys. Chem. C* **2020**, *124*, 12548-58. DOI
86. Wang, J.; Perry, N. H.; Guo, L.; Vayssieres, L.; Tuller, H. L. On the theoretical and experimental control of defect chemistry and electrical and photoelectrochemical properties of hematite nanostructures. *ACS. Appl. Mater. Interfaces*. **2019**, *11*, 2031-41. DOI PubMed
87. Ye, F.; Zhao, B.; Ran, R.; Shao, Z. Facile mechanochemical synthesis of nano SnO₂/graphene composite from coarse metallic Sn and graphite oxide: an outstanding anode material for lithium-ion batteries. *Chem. Eur. J.* **2014**, *20*, 4055-63. DOI PubMed
88. Mancipe, S.; Martínez, J. J.; Pinzón, C.; Rojas, H.; Solis, D.; Gómez, R. Effective photocatalytic degradation of Rhodamine B using tin semiconductors over hydroxalate-type materials under sunlight driven. *Catal. Today*. **2021**, *372*, 191-7. DOI
89. Baggetto, L.; Ganesh, P.; Meisner, R. P.; et al. Characterization of sodium ion electrochemical reaction with tin anodes: experiment and theory. *J. Power. Sources*. **2013**, *234*, 48-59. DOI
90. Lee, M. H.; Park, J. H.; Han, H. S.; et al. Nanostructured Ti-doped hematite (α -Fe₂O₃) photoanodes for efficient photoelectrochemical water oxidation. *Int. J. Hydrogen. Energy*. **2014**, *39*, 17501-7. DOI
91. Chae, S. Y.; Rahman, G.; Joo, O. Elucidation of the structural and charge separation properties of titanium-doped hematite films deposited by electrospray method for photoelectrochemical water oxidation. *Electrochim. Acta*. **2019**, *297*, 784-93. DOI
92. Lian, X.; Yang, X.; Liu, S.; et al. Enhanced photoelectrochemical performance of Ti-doped hematite thin films prepared by the sol-gel method. *App. Surf. Sci.* **2012**, *258*, 2307-11. DOI
93. Niu, Y.; Zhou, Y.; Niu, P.; Shen, H.; Ma, Y. Effects of Ti doping on hematite photoanodes: more surface states. *J. Nanosci. Nanotechnol.* **2019**, *19*, 3437-46. DOI
94. Barradas, N. P. Rutherford backscattering analysis of thin films and superlattices with roughness. *J. Phys. D.: Appl. Phys.* **2001**, *34*, 2109-16. DOI
95. Barradas, N. P.; García, N. C.; Redondo-cubero, A.; Shen, G.; Kung, P.; Pau, J. Analytical simulation of RBS spectra of nanowire samples. *Nucl. Instrum. Methods. Phys. Res. B*. **2016**, *371*, 116-20. DOI
96. Klahr, B.; Gimenez, S.; Fabregat-Santiago, F.; Hamann, T.; Bisquert, J. Water oxidation at hematite photoelectrodes: the role of surface states. *J. Am. Chem. Soc.* **2012**, *134*, 4294-302. DOI
97. Jrad, F.; Naceur, J. B.; Ouertani, R.; Chtourou, R. Photo-electrochemical impedance spectroscopy analysis of hydrothermally synthesized β -In₂S₃ thin film photo-anodes. *Physica. E*. **2019**, *114*, 113585. DOI
98. Katsuki, T.; Zahran, Z. N.; Tanaka, K.; et al. Facile fabrication of a highly crystalline and well-interconnected hematite nanoparticle photoanode for efficient visible-light-driven water oxidation. *ACS. Appl. Mater. Interfaces*. **2021**, *13*, 39282-90. DOI
99. Peerakiatkhajohn, P.; Yun, J. H.; Chen, H.; Lyu, M.; Butburee, T.; Wang, L. Stable hematite nanosheet photoanodes for enhanced photoelectrochemical water splitting. *Adv. Mater.* **2016**, *28*, 6405-10. DOI PubMed
100. Liu, G.; Karuturi, S. K.; Chen, H.; et al. Tuning the morphology and structure of disordered hematite photoanodes for improved water oxidation: a physical and chemical synergistic approach. *Nano. Energy*. **2018**, *53*, 745-52. DOI
101. Qin, D.; Li, Y.; Wang, T.; et al. Sn-doped hematite films as photoanodes for efficient photoelectrochemical water oxidation. *J. Mater. Chem. A*. **2015**, *3*, 6751-5. DOI
102. Bak, A.; Choi, W.; Park, H. Enhancing the photoelectrochemical performance of hematite (α -Fe₂O₃) electrodes by cadmium incorporation. *Appl. Catal. B. Environ.* **2011**, *110*, 207-15. DOI
103. Jha, B. K.; Chaule, S.; Jang, J. Enhancing photocatalytic efficiency with hematite photoanodes: principles, properties, and strategies for surface, bulk, and interface charge transfer improvement. *Mater. Chem. Front.* **2024**, *8*, 2197-226. DOI
104. Yoon, K.; Park, J.; Lee, H.; et al. Unveiling the role of the Ti dopant and viable Si doping of hematite for practically efficient solar water splitting. *ACS. Catal.* **2022**, *12*, 5112-22. DOI
105. Liu, H.; Fan, X.; Li, Y.; Guo, H.; Jiang, W.; Liu, G. Hematite-based photoanodes for photoelectrochemical water splitting: performance, understanding, and possibilities. *J. Environ. Chem. Eng.* **2023**, *11*, 109224. DOI
106. Jeon, T. H.; Moon, G.; Park, H.; Choi, W. Ultra-efficient and durable photoelectrochemical water oxidation using elaborately designed hematite nanorod arrays. *Nano. Energy*. **2017**, *39*, 211-8. DOI
107. Iandolo, B.; Zhang, H.; Wickman, B.; Zorić, I.; Conibeer, G.; Hellman, A. Correlating flat band and onset potentials for solar water splitting on model hematite photoanodes. *RSC. Adv.* **2015**, *5*, 61021-30. DOI
108. Toroker, M. C. Theoretical insights into the mechanism of water oxidation on nonstoichiometric and titanium-doped Fe₂O₃(0001). *J. Phys. Chem. C*. **2014**, *118*, 23162-7. DOI
109. Kamimura, J.; Bogdanoff, P.; Abdi, F. F.; et al. Photoelectrochemical properties of GaN photoanodes with cobalt phosphate catalyst for solar water splitting in neutral electrolyte. *J. Phys. Chem. C*. **2017**, *121*, 12540-5. DOI
110. Bartesaghi, D.; Pérez, I. C.; Kniepert, J.; et al. Competition between recombination and extraction of free charges determines the fill factor of organic solar cells. *Nat. Commun.* **2015**, *6*, 7083. DOI PubMed PMC
111. Dias, P.; Lopes, T.; Meda, L.; Andrade, L.; Mendes, A. Photoelectrochemical water splitting using WO₃ photoanodes: the substrate and temperature roles. *Phys. Chem. Chem. Phys.* **2016**, *18*, 5232-43. DOI
112. Krol, R.; Grätzel, M. Photoelectrochemical hydrogen production. 1th ed. New York: Springer; 2012. Available from: <https://link.springer.com/book/10.1007/978-1-4614-1380-6>. [Last accessed on 21 Mar 2025].
113. Yu, Q.; Meng, X.; Wang, T.; Li, P.; Ye, J. Hematite films decorated with nanostructured ferric oxyhydroxide as photoanodes for

- efficient and stable photoelectrochemical water splitting. *Adv. Funct. Materials.* **2015**, 25, 2686-92. [DOI](#)
114. Li, C.; Li, A.; Luo, Z.; et al. Surviving high-temperature calcination: ZrO₂-induced hematite nanotubes for photoelectrochemical water oxidation. *Angew. Chem. Int. Ed.* **2017**, 56, 4150-5. [DOI](#)
115. Zhang, R.; Fang, Y.; Chen, T.; et al. Enhanced photoelectrochemical water oxidation performance of Fe₂O₃ nanorods array by S doping. *ACS. Sustainable. Chem. Eng.* **2017**, 5, 7502-6. [DOI](#)